J. Onoe, *Bull. Soc. Discrete Variational Xα* **39** (No.1-2), 132–188 (2026).

Discrete-Variational Xα Molecular Orbital Approaches to Materials Science : A Review

–From Actinides to Functional and Environmental Materials–

Jun ONOE*

Department of Energy Science and Engineering, Nagoya University

*Corresponding author

Prof. Dr. Jun ONOE

Department of Energy Science and Engineering

Nagoya University

Furo-cho, Chikusa-ku, Nagoya, Aichi 464-8603, Japan

E-mail: j-onoe@energy.nagoya-u.ac.jp or onoe.jyun.r0@f.mail.nagoya-u.ac.jp

Abstract

Discrete-variational Xα molecular orbital (DV-Xα) method and its relativistic extension based on the discrete-variational Dirac-Slater (DV-DS) formalism provide useful frameworks for analyzing the electronic structures and chemical bonding of materials ranging from molecules to condensed matter. In contrast to conventional MO calculations that often require substantial computational resources for extended systems, the DV approach enables electronic-structure calculations for clusters containing transition-metal and heavy-element atoms and has therefore been applied extensively to materials containing localized d- and f-electrons. However, when used within the one-electron approximation, these methods cannot readily describe the multiplet structures and optical properties of the strongly correlated systems. DV-ME method, a first-principles many-electron approach, can explicitly describe the optical properties of the strongly correlated systems, and has been used successfully to analyze their multiplet energy levels and optical properties.

In this review, we summarize a series of studies employing DV-Xα/DV-DS/DV-ME approaches to elucidate the relationship among electronic structure, chemical bonding, spectroscopy, and materials properties. We initially focused on relativistic effects on electronic structures and chemical bonding in uranium compounds such as UF_6, UF_5, uranyl nitrate complexes, uranium carbide, metallic uranium, and uranium alloys. Particular attention was paid to the contribution of relativistic effects to orbital energies, bond formation, bond overlap populations, and molecular geometries. Thereafter, the atomic-number dependence of relativistic effects on chemical bonding was also systematically examined, providing a molecular-orbital-based interpretation of the origin of the unusual chemical properties of heavy elements.

These approaches were subsequently extended to uranium/transition-metal (TM) alloys, carbon clusters, TM ferrocyanides, and metal-ion complexes in nitric acid solutions. The combination of spectroscopic measurements with first-principles electronic-structure calculations enabled the chemical species of Ru, Rh, and Pd ions in aqueous nitric acid to be investigated at the molecular level. Furthermore, electronic-structure calculations were used to interpret the interaction between platinum-group-metal ions and Prussian-blue nanoparticles, providing a molecular-level basis for selective metal-ion uptake.

The evolution of these studies demonstrates that DV-Xα/DV-DS/DV-ME methods can serve not only as tools for interpreting electronic structures and spectra but also as a bridge between fundamental quantum chemistry and the design of functional materials for industrial applications.

Keywords: *DV-Xα/DV-DS/DV-ME methods*; *relativistic effects*; *multiplet, chemical bonding*; *actinides*; *uranium*; *XPS*; *nanocarbons*; *Prussian blue*; *platinum-group metals*; *nuclear waste*; *materials science*

1. Introduction

Understanding the relationship between electronic structure and macroscopic properties is one of the central objectives of materials science. In particular, the chemical and physical properties of materials containing transition metals, lanthanides, and actinides are strongly influenced by localized d- and f-electrons, orbital hybridization, electron correlation, and relativistic effects. Theoretical descriptions of these systems therefore require computational approaches that can accurately treat the electronic structures of relatively complex atomic arrangements while providing chemically meaningful insights on individual atomic orbitals.

DV-Xα method, originally developed as a cluster-based molecular-orbital method within the framework of the Xα approximation [1, 2], has been extensively applied for the analysis of electronic structures, chemical bonding, and spectroscopic properties of molecules and solids [3–8]. One of its major advantages of the method is that it provides chemically intuitive quantities such as orbital populations, bond overlap populations, and atomic-orbital contributions to molecular orbitals.

The relativistic effects become increasingly important for heavy elements [9, 10]. Figure 1 schematically illustrates how relativistic effects influence the energies and spatial distributions of atomic orbitals.

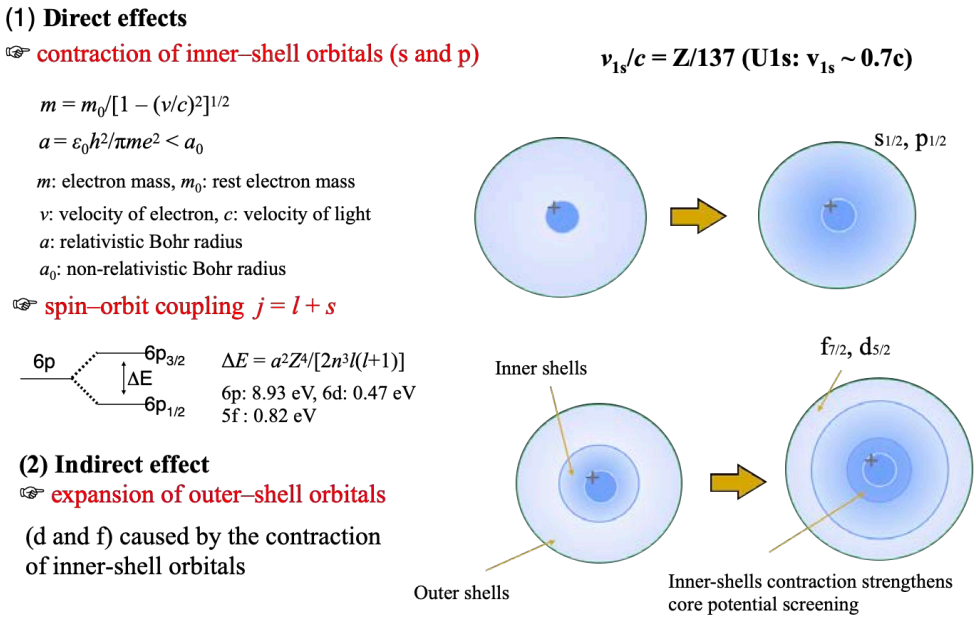


Figure 1. Schematic illustration of relativistic effects on atomic orbitals: (1) Direct effects such as the contraction of inner-shell AOs (s and p orbitals) and spin-orbit coupling (for an example, 6p AO splits to $6p_{1/2}$ and $6p_{3/2}$ AOs), (2) Indirect effect such as expansion of outer-shell AOs (d and f orbitals).

Prior to discussing relativistic effects in molecules and solids, we first consider their influence on atomic electronic structure. Within the nonrelativistic Bohr model, the Bohr radius (a) and the energy (E) of a hydrogen-like atom are given by the following equations,

$$a = \frac{n^2\hbar^2}{mZe^2} \qquad (1),$$

and

$$E = -\frac{me^2}{2\hbar^2}\frac{Z^2}{n^2} \qquad (2).$$

Here, m is the mass of electron, n is the principal quantum number, Z is the atomic number, e is the elementary charge, $\hbar$ is Dirac constant. For a hydrogen-like atom, the ratio of the electron velocity in the 1s electron (υ_{1s}) to the speed of light (c) is approximately given by Z/137. For uranium (Z=92), this ratio reaches approximately 0.67, indicating that relativistic effects cannot be neglected in describing its electronic structure. Even for the U6s valence orbital, the υ_{6s} is estimated to be 0.1c, suggesting that relativistic effects can significantly affect the valence electrons involved in chemical bonding. According to the theory of relativity, the velocity-dependent relativistic mass (m) can be expressed as,

$$m = m_0/[1 - (\upsilon/c)^2]^{1/2} \qquad (3).$$

Here, m_0 and υ are the rest mass and velocity of electron, respectively. This relationship illustrates that the effective inertial mass increases with electron velocity. Accordingly, eqs. (1) and (2) show that a and E become contracted and increased, respectively, with increasing Z. These changes become particularly pronounced for heavy elements.

As illustrated in Fig. 1, relativistic effects on AOs can be classified into two categories: direct and indirect effects. The former effects lead to the contraction of inner-shell orbitals (*e.g.* $s_{1/2}$ and $p_{1/2}$ orbitals). Furthermore, the total angular momentum quantum number j (= $l \pm 1/2$) plays a fundamental role in Dirac formalism, naturally accounting for energy splitting arising from spin-orbit interactions (*e.g.* 6p oribital splits to $6p_{3/2}$ and $6p_{1/2}$ components). In contrast, indirect relativistic effects lead to the expansion of outer d and f AOs. This expansion arises primarily from the increased screening of the nuclear charge resulting from the contraction of inner-shell orbitals. As described above, these relativistic effects become increasingly pronounced with increasing Z, significantly affecting the valence electronic structures and chemical bonding of molecules, complexes, and solids containing heavy elements such as uranium.

Figure 2 compares the nonrelativistic and relativistic radial wave functions, [rR(r)], of the valence AOs of uranium atom [13]: (a) U5f, (b) U6s, (c) U6p, and (d) U6d. One can find the expansion of the $5f_{5/2}$ and $5f_{7/2}$ orbitals due to the indirect relativistic effect, and the pronounced contraction of the $6s_{1/2}$ and $6p_{1/2}$

orbitals due to the direct relativistic effect. The $6p_{3/2}$ orbital exhibits little change relative to the nonrelativistic 6p orbital. Both $6d_{3/2}$ and $6d_{5/2}$ orbitals are a little contracted, so that an increase in their radial wave function amplitudes in the U–F bond region (r < 3.778 au), when compared to the nonrelativistic 6d orbital. These results demonstrate that the contraction and expansion of the atomic orbitals due to the relativistic effects depend on the total angular momentum j.

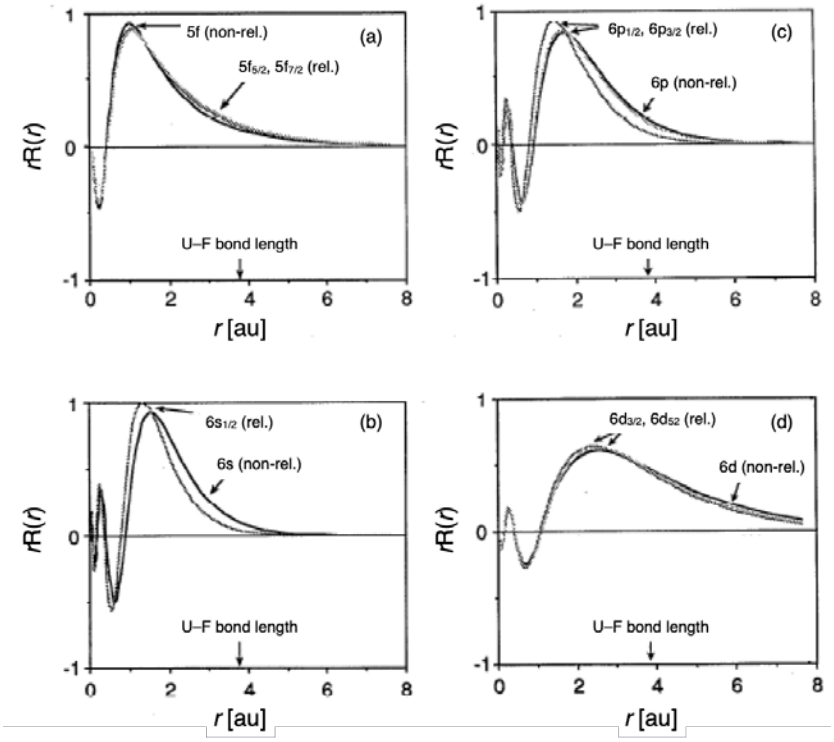


Figure 2. Comparison between non-relativistic and relativistic radial wave functions, [rR(r)], of the valence AOs for uranium atom: (a) U5f, (b) U6s, (c) U6p, and (d) U6d. (FIG. 3 of Ref. 13 was partially modified.)

At what atomic number do relativistic effects become important for the electronic structure and chemical bonding of molecules, complexes, and solids? We investigated atomic-number (Z) dependence of the chemical bonds of hexafluorides, XF_6 (X = S, Se, Mo, Te, W, U), using nonrelativistic DV-HFS and relativistic DV-DS methods [14]. Figure 3 shows (a) Z-dependence of bond overlap populations ($P_{X\text{-}F}$) of XF_6 (X = S, Se, Mo, Te, W, U) obtained using the nonrelativistic and relativistic methods, and (b) plot of the difference ($\Delta P_{X\text{-}F}$) in $P_{X\text{-}F}$ between relativistic and nonrelativistic calculations as a function of Z^2. Here, $P_{X\text{-}F}$ was estimated using Mulliken population analysis. As shown in Fig. 3a, it is interesting to note that the relativistic effects on the X-F chemical bonding become particularly pronounced in the hexafluoride

molecules containing an element with Z larger than 50 (Te, W, and U). Hence, the nonrelativistic calculations may be inadequate to describe the chemical bonding in molecules containing such heavy elements. These results are essentially applicable to other molecules and solids. Namely, Figure 3 suggests that the relativistic MO calculations should be used to study the bond nature in molecules containing elements with Z exceeding 50. As shown in Fig. 3b, the $\Delta P_{X\text{-}F}$ exhibits an approximately linear dependence on Z^2 for the hexafluorides except UF_6, and is consistent with Z^2 dependence of the relativistic contraction of the bond distances for the hydrides reported by Pyykkö *et al* [9]. Consequently, the Z-dependence of the relativistic effects on chemical bonding in terms of bond overlap populations is corresponding to that of the relativistic effects on the bond distances with analysis of bonding energy. As shown in Fig. 3b, Z^2 dependence is not valid for UF_6. Since the other actinide hexafluorides such as NpF_6 and PuF_6 have the large $\Delta P_{X\text{-}F}$ values as much as that for UF_6, relativistic effects for 5f-electron system cannot be described solely by the Z^2 dependence. Although Pyykkö *et al*. have not shown the reason behind the Z^2 dependence of bond distances for the hydrides, we have explained the Z dependence of $\Delta P_{X\text{-}F}$ for the hexafluorides including UF_6 by the simple model based on Z dependence of the relativistic effects on the 1s atomic orbital for a hydrogenic atom. Details have been discussed elsewhere [15].

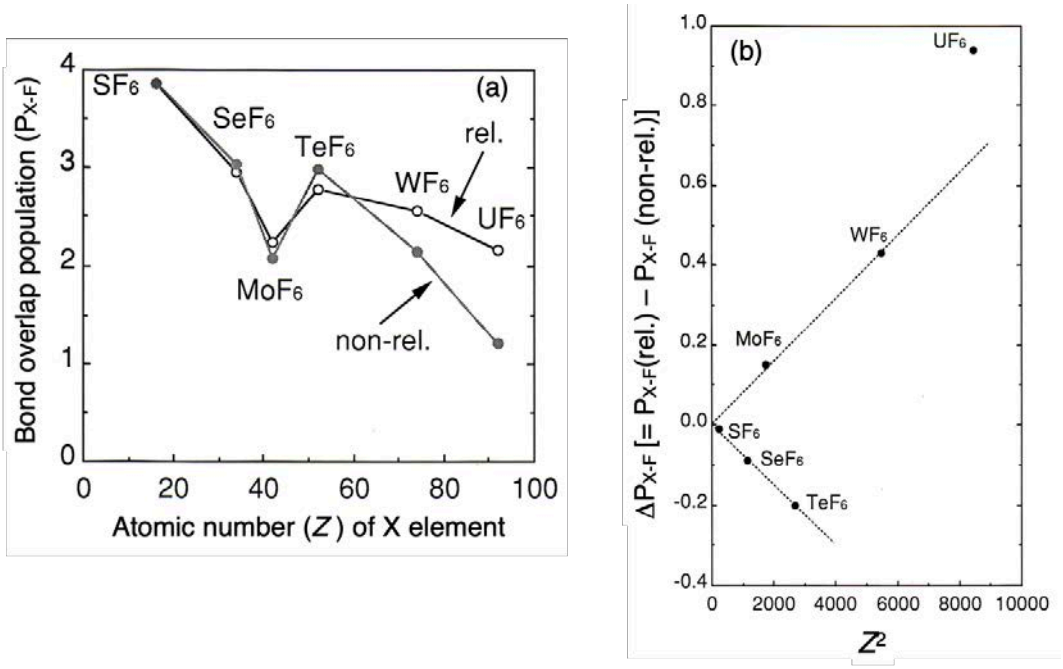


Figure 3. (a) Atomic-number (Z) dependence of bond overlap populations ($P_{X\text{-}F}$) for hexafluorides (XF_6: X = S, Se, Mo, Te, W, U), obtained using the non-relativistic DV-HFS and relativistic DV-DS methods, (b) Plot of the difference ($\Delta P_{X\text{-}F}$) in $P_{X\text{-}F}$ between relativistic and non-relativistic calculations as a function of Z^2.

We initially investigated relativistic effects on the electronic structure and chemical bonding of UF_6 and UF_5 molecules [11–13, 16, 17], uranium complexes [18–21], and uranium compounds [22–27], using DV-Xα/DV-DS methods. Subsequently, we applied DV-Xα method to nanocarbon materials [28]. More recently, we investigated the electronic structures (multiplet energy levels) and functional properties of transition-metal-containing materials [29–32], and metal-ion uptake and separation in aqueous systems [33], using DV-ME method in combination with the other first-principles calculations.

The purpose of this review is to provide a systematic overview of these studies from the perspective of relationships among electronic structure–chemical bonding–functional properties. Rather than presenting the individual studies chronologically, we emphasize the progressive expansion of the DV-Xα/DV-DS/DV-ME methods from fundamental aspects to spectroscopy, structural and functional materials, and nuclear-waste/resource-recovery applications.

2. Computational

2.1. Discrete-variational Hartree-Fock-Slater (Xα) and Dirac-Slater molecular orbital methods

The DV-DS method has been demonstrated to be a powerful tool for investigating the electronic structures of molecules containing heavy elements, such as uranium [11–27]. The one-electron molecular Hamiltonian (**H**) in the DV-DS method is expressed as,

$$\mathbf{H} = c\boldsymbol{\alpha}\mathbf{P} + \boldsymbol{\beta}mc^2 + V(r) \qquad (4).$$

Here, c, $\mathbf{P}$, m, $\boldsymbol{\alpha}$/$\boldsymbol{\beta}$, and $V(r)$ denote the speed of light, the momentum operator, the electron rest mass, the Dirac matrices, and the sum of Coulomb and exchange potentials, respectively. The molecular orbitals (MOs) are constructed as linear combinations of atomic orbitals (AOs). Further details of the DV-DS method have been reported elsewhere [13, 34].

The DV-DS and DV-HFS methods employed in the present review are briefly outlined below. In both methods, the molecular wave functions are expressed as linear combinations of AOs obtained by numerically solving the Dirac-Slater or Hartree-Fock-Slater equations, respectively, using atomic-like potentials derived from the molecular potential. Consequently, the AOs employed as basis functions are adapted to optimized to molecular environment, providing sufficient flexibility for describing the formation of MOs. The matrix elements in the secular equation,

$$(\mathbf{H} - E\mathbf{S})\mathbf{C} = 0 \qquad (5),$$

were evaluated by calculating weighted sum of the integrand values at DV sample points. Two-center (overlap) charge densities are partitioned into one-center (atomic) charges using Mulliken population

analysis [35] in the self-consistent charge (SCC) method [36] which was used to approximate the complete self-consistent field. The atomic potentials used to generate the basis functions are constructed from the spherical averages of the molecular charge densities around the nuclei, with the contributions from the potential tails of neighboring atoms taken into account. Further computational details of the two methods employed in this review have been described elsewhere [3, 34]. Nakamatsu *et al.* demonstrated that the electronic structures calculated using the DV-DS and DV-HFS methods are in good agreement for molecules composed of light elements, such as CF_4 and SF_6 [37], for which relativistic effects are negligibly small.

2.2. Chemical bonding analysis

One of the important advantages of the DV-Xα/DV-DS approach is that the calculated wave functions can be analyzed in terms of bond overlap populations (BOPs) based on Mullliken population analysis [35]. In this analysis, the total electron population is partitioned into the gross populations of individual AOs. The gross population (n_i) of the *i*-th AO is given by,

$$n_i = \sum_{(l,j)} \varphi_l C_{il} C_{jl} S_{ij}, \qquad (6).$$

Here, φ_l is the occupancy of the *l*-th MO, $C_{il}(C_{jl})$ is the coefficient of the linear combination of AOs, and S_{ij} is the overlap integral between the *i*-th and *j*-th AOs. Two-center charges are estimated from the overlap populations defined as,

$$n_{ij} = \sum_{(l)} \varphi_l C_{ij} C_{jl} S_{ij}. \qquad (7).$$

Positive overlap populations generally indicate bonding interactions, whereas small or negative values suggest weak bonding or antibonding interactions, respectively. This analysis is particularly useful for investigating relativistic effects because it enables changes in chemical bonding to be interpreted in terms of the contributions of individual AOs and their interactions. In this way, the relationship between relativistic changes in atomic orbitals and the resulting changes in chemical bonding and bond lengths can be examined.

3. Relativistic Effects on electronic structure and chemical Bonding

3.1. Electronic structure of UF_6

UF_6 molecule is a key material used in ^{235}U enrichment for nuclear fuel production by gas centrifugation. The valence electronic structure of UF_6 has been investigated using the DV-DS method, and the calculated results have been compared with experimental results obtained using x-ray photoelectron spectroscopy (XPS) [11, 16]. The calculations reproduced the major features of the experimental valence spectrum and enabled the observed photoelectron peaks to be assigned to specific molecular orbitals (see Table 1 in Ref. 16).

Figure 4 shows (a) a comparison in one-electron energies for the ground-state levels obtained between the nonrelativistic (DV-HFS) and the relativistic (DV-DS) methods, (b) a schematic energy diagram illustrating the correlation among the lower-lying valence MOs, U and F AOs, (c) the valence photoelectron spectra of UF_6 in a binding-energy range of 0–50 eV: (top) experimental valence photoelectron spectrum of gaseous UF_6 [38]; (middle) theoretical ionization energies and XPS intensities (the height of each vertical line proportional to the corresponding intensity), where XPS intensity was estimated using the equation proposed by Gelius [39]; (bottom) theoretical valence electron spectrum, which was obtained by replacing each level in Fig. 4b as a Lorentzian curve with FWHM (full width of half maximum) of 0.4 eV (for the $12\gamma_{8u}$ to $9\gamma_{8g}$ MOs) and 1.0 eV (for the $9\gamma_{8u}$ to $7\gamma_{6u}$ MOs) estimated from the experimental FWHMs of peaks 1 and 6, respectively. The energy scale of the calculated spectra was shifted by +1.28 eV in order that the first ionization energy coincided with the experimental value of 14.14 eV.

Peak 6 in the experimental spectrum is assigned to the $9\gamma_{8u}$ level which has the U6p AO as a main contribution. The calculated ionization energies for the levels, $8\gamma_{6u}$, $8\gamma_{6g}$, $8\gamma_{8g}$, and $8\gamma_{8u}$, containing the F2s AO as a main component were approximately 3 eV lower than the experimental values of the F2s energy for peaks 7 and 8. A similar systematic deviation has also been reported in the case of SF_6 [40]. It has been found that the Xα and local-density functional exchange potentials result in 3 eV lower ionization energy of the F2s than the experimental one, even for an isolated F atom. When peaks $8\gamma_{6u}$–$8\gamma_{8u}$ are shifted by 3 eV to higher binding energies, peak 7 can be assigned to $8\gamma_{6u}$. The intense peak 8 is found to consist of the $8\gamma_{6g}$ and $8\gamma_{8g}$ levels, whereas peak 9 is assigned to the $8\gamma_{8u}$ level. The shoulder (peak 10) on the higher-binding-energy side of peak 9 originates from the $7\gamma_{6u}$ level. The theoretical spectrum (bottom of Fig. 4c) reproduces the main features of the experimental one. More details of the differences in relative XPS intensities between experimental (top) and theoretical (bottom) results have been discussed in Ref. 11. We obtained no MOs corresponding to peaks A and B shown in Fig. 4c (top). In Ref. 38, Mårtensson *et al.* did not discuss the origins of the peaks. In their experiments, commercially obtained UF_6 was introduced into the sample compartment without further purification. Because HF is known to be

a major impurity in UF_6 when it is used without additional purification [41], peaks A and B may originate either from this impurity or from satellite peaks associated with the relaxation processes of the excited valence level, and not be caused by the photoelectron directly arising from the valence levels of UF_6.

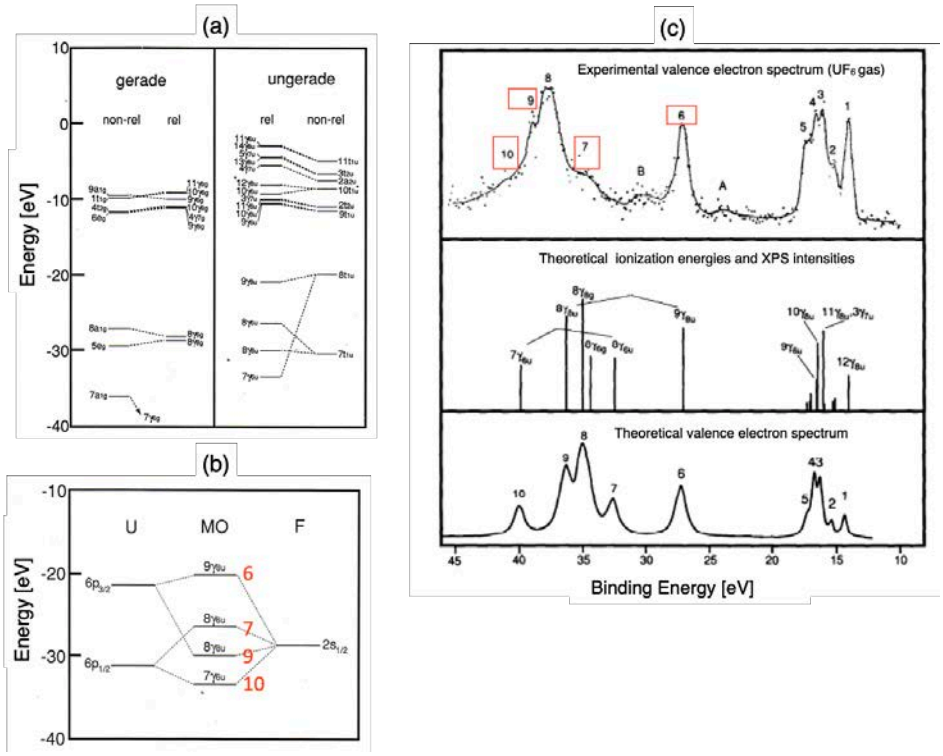


Figure 4. (a) Comparison in one-electron energies for the ground-state levels obtained between the nonrelativistic and relativistic methods, (b) Schematic energy diagram representing the correlation among the lower-lying valence MOs along with U and F AOs, (c) Valence photoelectron spectrum of UF_6 in a binding-energy range of 0–50 eV: experimental valence photoelectron spectrum of gaseous UF_6 [38] (top); theoretical ionization energies and XPS intensities (the height of each vertical line proportional to the corresponding intensity) (middle); theoretical valence electron spectrum (bottom).

We have shown that four MOs (see Fig. 4b) arise primarily from interactions between U6p and F2s AOs, whereas $8\gamma_{6g}$, $8\gamma_{8g}$, and $8\gamma_{8u}$ levels are mainly dominated by F2s AO (Table 1 in Ref. 13). Namely, the four MO levels originate from interactions between U($6p_{1/2}$ and $6p_{3/2}$) and $F2s_{1/2}$, as shown in Fig. 4b. By comparing the orbital components and bonding characteristics of these MO levels with the valence AOs, we identified that the $7\gamma_{6u}$ and $8\gamma_{6u}$ levels form the bonding–antibonding pair composed of the $U6p_{1/2}$ and $F2s_{1/2}$ AOs, while the $8\gamma_{8u}$ and $9\gamma_{8u}$ levels constitute the bonding–antibonding pair composed of the $U6p_{3/2}$ and $F2s_{1/2}$ AOs. Consequently, peaks 6 and 9 are assigned to be the antibonding–bonding pair due to the $U6p_{3/2}$–$F2s_{1/2}$ interaction, while peak 7 and shoulder 10 are assigned to the pair due to the $U6p_{1/2}$–$F2s_{1/2}$

interaction. Hence, peaks 6, 7, 9, and shoulder 10 shown in Fig. 4a (top) lie under the large spin-orbit interaction of the U6p AO. This finding suggests that many-body effects play a relatively minor role in determining the spectral features in this energy region. Details of the molecular effects on U6p spin-orbit coupling between the $9\gamma_{8u}$ and $7\gamma_{6u}$ MOs have been discussed in Ref. 16.

3.2. UV-excited states of UF_6

The UV absorption spectrum of UF_6 is well known to exhibit two characteristic bands, A-X (340–420 nm) and B-X (200–340 nm) bands [42], as shown in Fig. 5. In addition, exciting the A-X band leads to fluorescence ($UF_6^* \rightarrow UF_6 + h\nu$), whereas exciting the B-X band to dissociation ($UF_6^* \rightarrow UF_5 + F$) [see the related references cited in Ref. 12]. However, the reason why excitation in the two bands leads to these different deactivation processes has not yet been fully understood. To address this issue, we performed the DV-DS MO calculations, and demonstrated that the bonding characteristics of UF_6 differ significantly between the relativistic and nonrelativistic MO calculations. Table 1 compares the excitation energies of charge-transfer transitions of UF_6 with the experimental values, along with the other theoretical works. The $12\gamma_{8u}$ MO is the highest occupied molecular orbital (HOMO). The theoretical excitation energies in the present work agree well with experimental values within 0.3 eV, which is better than those in the other theoretical works. Figure 5 compares the calculated excitation energies with the experimental UV absorption spectrum [42]. Here, the dashed lines represent experimental values assigned by Lewis *et al* [43], and the levels marked with an asterisk belong to the electric dipole-allowed transition. All theoretical excitation energies obtained in the present work successfully reproduce the fine structures of UV absorption spectrum.

As shown in Table 1 and Fig. 5, the A-X (420-340 nm) band, which exhibits relatively weak absorption, consists of only one magnetic-dipole-allowed transition, $12\gamma_{8u} \rightarrow 4\gamma_{7u}$, whereas numerous electric-dipole-allowed transitions contribute to the B-X band, resulting in its intense absorption. To understand the difference in UF_6 deactivation processes following excitation into A-X and B-X bands, we evaluated the changes in the U–F total bond overlap populations between the ground and excited states (hereafter denoted as $\Delta P_{U\text{-}F}$). The calculated values are also listed in Table 1. We used $\Delta P_{U\text{-}F}$ as an indicator of the tendency toward U–F bond dissociation, with a larger negative value indicating a greater tendency for bond dissociation in the excited UF_6. The first two transitions originating from the level $12\gamma_{8u}$ are therefore not expected to induce dissociation, because their $\Delta P_{U\text{-}F}$ are essentially zero, whereas the other transitions exhibit substantially negative $\Delta P_{U\text{-}F}$ values, indicating a pronounced tendency toward U–F bond dissociation.

To further clarify the difference in the deactivation processes following excitation into the A-X and B-X bands, we evaluated the U–F bond overlap population associated with each MO in the ground state.

Table 1. Theoretical excitation energies of charge transfer transitions of UF_6 compared with the experimental values, along with the other theoretical works. The reference numbers correspond to those cited in Ref. 12.

Transition types	Electric dipole-allowed	Magnetic dipole-allowed	Theoretical (eV)					Experimental (eV)	ΔP_{U-F} [c]
			DV-DS (TS)			RXα-SO [a]	ab initio [d]		
			this work	ref. [12]	ref. [11]				
$12\gamma_{8u}$–$4\gamma_{7u}$	no	yes	3.06	2.78	3.67	3.34	3.41–3.55	3.04 [d]	−0.04
$12\gamma_{8u}$–$13\gamma_{8u}$	no	yes	4.02	3.72	4.43	4.08	4.01	3.76 [d]	−0.04
$12\gamma_{8u}$–$5\gamma_{7u}$	no	yes	4.15	3.94	4.59	4.16	4.56	3.98 [d], 3.87 [e]	−0.11
$11\gamma_{8g}$–$4\gamma_{7u}$	yes	no	4.21	4.05	4.95	4.53	5.37	4.05 [d], 4.13 [e]	−0.43
$10\gamma_{6g}$–$4\gamma_{7u}$	no	no	4.25	4.08	5.01	4.56	5.39		−0.43
$10\gamma_{6u}$–$4\gamma_{7u}$	no	no	4.32		4.91				−0.27
$3\gamma_{7u}$–$4\gamma_{7u}$	no	yes	5.03		5.16				−0.46
$11\gamma_{8g}$–$13\gamma_{8u}$	yes	no	5.04	4.89	5.71	5.14	5.96	4.77 [d,e]	−0.52
$11\gamma_{8u}$–$4\gamma_{7u}$	no	yes	5.15		5.60				−0.46
$12\gamma_{8u}$–$14\gamma_{8u}$	no	yes	5.18	5.22	5.64	5.57	5.24		−0.26
$10\gamma_{6u}$–$13\gamma_{8u}$	no	yes	5.26		5.67				−0.36
$12\gamma_{8u}$–$11\gamma_{6u}$	no	yes	5.28	5.38	5.80	5.42	6.02		−0.24
$11\gamma_{8g}$–$5\gamma_{7u}$	yes	no	5.40	5.04	5.88	5.32	6.40		−0.53
$10\gamma_{6g}$–$13\gamma_{8u}$	yes	no	5.51	4.92	5.76				−0.55
$10\gamma_{8u}$–$4\gamma_{7u}$	no	yes	5.55	4.02	5.85	4.55	5.83		−0.50
$11\gamma_{8u}$–$13\gamma_{8u}$	no	yes	5.98		6.36				−0.58
$10\gamma_{8g}$–$4\gamma_{7u}$	yes	no	5.99		6.41			5.72 [e], 5.80 [d]	−0.46
$3\gamma_{7u}$–$13\gamma_{8u}$	no	yes	6.02		6.27				−0.58
$4\gamma_{7g}$–$4\gamma_{7u}$	yes	no	6.03		6.21				−0.60
$3\gamma_{7u}$–$5\gamma_{7u}$	no	yes	6.11		6.44				−0.52
$11\gamma_{8u}$–$5\gamma_{7u}$	no	yes	6.12		6.52				−0.53

[a] Ref. [25]. [b] Ref. [13].
[c] The values are the differences in U–F bond overlap populations between the excited and ground states.
[d] Ref. [26]. [e] Ref. [1].

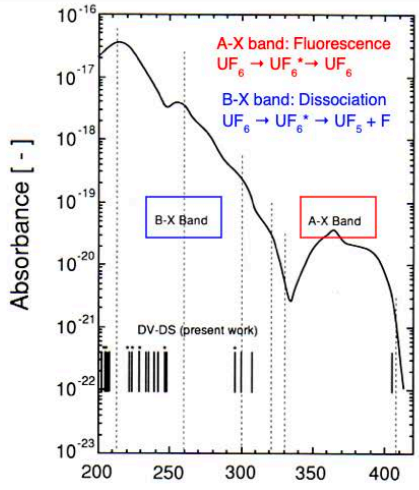


Figure 5. Comparison of excitation energies corresponding to F2p–U5f charge-transfer transitions between the present work and the experimental UV absorption spectrum of UF_6 [42].

These results indicate that the distinct dissociation behaviors between the A-X and B-X bands comes from the bonding nature for the levels in the ground state. The U–F bond overlap population of the level $12\gamma_{8u}$ (HOMO) is obtained to be –0.54, indicating an antibonding character between U and F atoms. The main component of $12\gamma_{8u}$ is the U6p AO lying energetically below F2p AO, which contributes to the antibonding *via* an interaction with the latter. The level $10\gamma_{6u}$ is also antibonding. The overlap population for the levels $11\gamma_{8g}$ and $10\gamma_{6g}$ composed exclusively of the F2p AO is almost zero, which indicates that these levels are nonbonding. The other levels below those are bonding, because they have positive overlap population. The unoccupied levels in Table 1 have the large 5f AO component as a main contribution and have antibonding characters, except for the almost nonbonding level $4\gamma_{7u}$ (LUMO: lowest unoccupied molecular orbital). From the ΔP_{U-F} and the bonding character of each MO, the difference in the deactivation process between the A-X and B-X bands can be qualitatively explained as follows. For the A-X band, since the excitation from the HOMO to the LUMO is the transition from an antibonding level to a nonbonding one, the excitation does not induce the antibonding interaction between the U and F atoms. Indeed, the ΔP_{U-F} is essentially zero. On the other hand, the excitations in the B-X band remarkably increase the antibonding interaction between the U and F atoms, because most of them belong to the transitions from bonding to antibonding orbitals. The initial levels with antibonding and

nonbonding characters also participate in the excitations of the B-X band. Even for such excitations, the overall changes in U–F bonds show a large increase in the antibonding interaction, since the final levels on the excitation have antibonding character to a great extent. Consequently, the changes in the overlap population can explain the experimental fact that the excitations in the A-X band cause fluorescence without dissociation, differing from the others.

3.3. Relativistic effects on chemical bonding in UF_6

As described in Fig. 2, the valence AOs of uranium are strongly affected by relativistic effects. Thus, the chemical bonding of uranium is easily considered to be influenced by the effects, as shown in Fig. 3. In this section, we examined the role of individual valence AOs in the relativistic effects on the chemical bonding of UF_6 by comparing the results obtained using DV-HFS and DV-DS methods [13].

To investigate how the relativistic effects influence the interatomic interactions, we summed the bond overlap populations over the MO levels and evaluated the total contribution from each AO. Table 2 shows these overlap populations obtained from the nonrelativistic and relativistic calculations. The bond overlap population provides an indicator of the nature of the U–F interaction: a negative value indicates an antibonding interaction, a positive value indicates a bonding interaction, and a value close to zero indicates a nonbonding interaction.

Table 2. Comparison in U-F overlap populations between the nonrelativistic DV-HFS and relativistic DV-DS calculations [13].

		DV-HFS (nonrelativistic) F		DV-DS (relativistic) F	
		2*s*	2*p*	2*s*	2*p*
U	5*f*	0.07	1.07	0.08	1.17
	6*s*	−0.16	−0.54	−0.05	−0.29
	6*p*	−0.56	−0.71	−0.42	−0.85
	6*d*	0.18	1.54	0.16	1.77
Total U–F bond overlap population		+1.21		+2.15	

The U–F bond overlap population for the relativistic case was +2.15. On the other hand, the value for the nonrelativistic case was found to be +1.21, which is about half of the value for relativistic case. This indicates that the chemical bonding of UF_6 molecule cannot be discussed without the relativistic effects. Each pair of atomic orbitals makes a different contribution to the U–F bond. In the nonrelativistic results,

the interactions of U5f–F2s/2p, and U6d–F2s/2p are found to be bonding, whereas the others are antibonding. These interactions between U and F atoms are qualitatively explained from the energy relation between the atomic and molecular orbitals. Since the F2s/2p levels are located below the HOMO $12\gamma_{8u}$, and the U5f/6d levels are located above it, the interaction between these F and U atomic orbitals leads to bonding MOs with the major components of the F2s/2p. On the other hand, the U6s/6p orbitals are located below the HOMO as well as the F2s/2p, so that these orbitals provide no bonding interaction as a total. In the present nonrelativistic result, the overlaps between the U6s/6p and F2s/2p are so large as to induce the remarkable repulsive interaction. Therefore, the bond overlap population for the nonrelativistic case is only half of the value for the relativistic one. From the overlap populations and the radial wave functions as shown in Fig. 2, the expansion and contraction of the uranium AOs due to the relativistic effects contribute significantly to the U–F bond formation. Since the indirect relativistic effects make both $5f_{5/2}$ and $5f_{7/2}$ AOs expanded to some extent, U5f–F2s and U5f–F2p bonding interactions become somewhat stronger than those in the nonrelativistic results. Indeed, the overlap populations of U5f–F2s and U5f–F2p interactions increase to 0.08 and 1.17 for the relativistic case, respectively, when compared to those of 0.07 and 1.07 for the nonrelativistic case. The antibonding interactions between U6s and F2s/2p AOs become weaker in the relativistic case, because the low-*j* $6s_{1/2}$ orbital is remarkably contracted by the direct relativistic effect as shown in Fig. 2b. This orbital contraction reduces the antibonding interactions between U6s and F2s/2p AOs. Although the radial distribution of relativistic U6d orbital is contracted, the overlap population between U6d and F2s/2p AOs increases, contrary to the case for the U6s. Owing to the relativistic contraction, the magnitude of the U6d wave function in the region between U and F atoms increases and the overlap population between the U6d and F2s/2p AOs correspondingly increases.

From the above results, the relativistic effects in the U–F bond formation can be summarized as follows. The expansion and contraction of AOs due to the relativistic effects result in the decrease in the repulsive interactions between U and F electron-occupied orbitals and lead to an increase in the bonding interactions between U and F bonding-antibonding pairs. The variation of interactions in terms of the U–F bond overlap populations can be examined as a function of the U–F interatomic distance for the nonrelativistic case. The U–F bond is stable for the longer U–F distance than the actual U–F bond length (3.778 au) at equilibrium. Namely, then U–F bond overlap population is +1.21 for the U–F distance of 3.778 au, decreases to –0.09 at 3.278 au and increases to +2.10 at 4.278 au. This result indicates that the increase in the U–F distance reduces the repulsive interactions (U6p–F2p, U6s–F2p, etc.) in the nonrelativistic case. Consequently, the relativistic effects strengthen the U–F bond and make the U–F bond-length contracted.

Finally, we evaluated the first ionization and HOMO–LUMO excitation energies for UF_6, and obtained those to be 12.86 eV and 3.06 eV, respectively, which are in good agreement with the experimental values of 14.14 eV and 3.04 eV, respectively. The role of individual valence AOs in the relativistic effects on chemical bonding of molecules has been discussed in detail elsewhere [44–46].

3.4. Bond nature of UF_5 monomer

The geometry of UF_5 monomer, which is formed by the UV photolysis of UF_6 in an argon matrix, has been investigated using IR and Raman spectroscopy [47–49]. The equilibrium geometry of the monomer was determined to be a square-pyramidal structure with C_{4v} symmetry with U–F(axial) and U–F(equatorial) bond lengths of 2.00 and 2.02 Å, respectively, and F(axial)–U–F(equatorial) bond angle of 101°. On the other hand, Wadt and Hay performed MO calculations of the geometry and electronic structure of the UF_5 monomer using the Hartree-Fock method with a relativistic effective core potential approximation [50]. They showed that the C_{4v} structure is slightly more stable, by approximately 1 kcal/mol (0.04 eV), than that with D_{3h} structure in the presence of spin-orbit interaction. The distinct difference between the two structures is that the UF_5 monomer with C_{4v} structure has a permanent dipole while that with D_{3h} structure does not. According to their report, the stabilization energy due to the dipole moment interacting with the surrounding inert-gas matrix was estimated to be less than 0.2 kcal/mol corresponding to a thermal energy at approximately 100 K. Since the experiments described above were conducted at less than 20 K, the C_{4v} geometry could remained trapped in the C_{4v} geometry without converting to the D_{3h} geometry. In the gas phase at room temperature, the UF_5 monomer may adopt a different geometry such as D_{3h} rather than C_{4v} geometry. Based on these considrations, Wadt and Hay concluded that the structure of the UF_5 monomer is fluxional between the C_{4v} and D_{3h} geometries, as illustrated in Fig. 6.

Why does the uranium atom exhibit such flexibility in its bonding in response to changes in molecular geometry? Although previous studies have shown that the two geometries have nearly values of orbital population and total energy, they did not provide a qualitative interpretation on the origin of the fluxional structure of the UF_5 monomer.

The aim of the present work is to address this question. In order to discuss the flexible bond of the UF_5 monomer, we examined the relationship between molecular geometry and chemical bonding of UF_5 using the bond overlap population. The bond overlap population and valence level structures of the monomer with the C_{4v} and D_{3h} geometries (see Figure 6) were investigated using the nonrelativistic DV-HFS and relativistic DV-DS methods.

Table 3 shows the bond overlap populations (P_B) between U and F atomic orbitals obtained from the two

calculations. It is found that the nonrelativistic calculation provides less than half of the bond overlap populations obtained by the relativistic calculation for both U–F_{eq} and U–F_{ax} interactions. This indicates that the relativistic calculation should be used in the study of the chemical bonding in actinide compounds [13]. In order to investigate the contribution of the U5f AO to the U–F bond formation, the P_B values between U and F valence AOs were examined using both nonrelativistic and relativistic calculations.

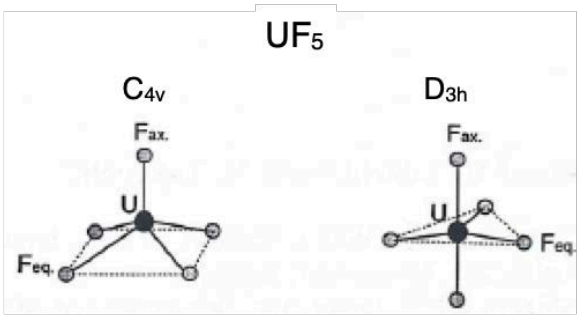


Figure 6. Schematic illustration of C_{4v} (U-F_{ax} = 2.00 Å, U-F_{eq} = 2.02 Å, F_{ax}-U-F_{eq} = 101°) and D_{3h} (U-F_{ax} = 2.00 Å, U-F_{eq} = 2.02 Å, F_{ax}-U-F_{eq} = 90°) geometries, which were experimentally and theoretically determined, respectively, for UF_5 molecule

Table 3. Bond overlap populations between U and F valence AOs obtained using DV-HFS (nonrel) and DV-DS (rel) calculations for UF_5 with C_{4v} symmetry

		bond overlap population	
		F_{eq}	F_{ax}
nonrel	U	+0.63	+0.11
rel	U	+1.43	+0.36

In the relativistic claculation, it is found that the U5f–F2s/2p interactions (P_B =1.11) contribute significantly to the U–F bond in addition to the U6d–F2s/2p ones (P_B = 1.66). On the other hand, the nonrelativistic calculation shows that the U6d–F2s/2p interactions (P_B = 1.49) mainly contribute to the U–F bond formation, while the U5f atomic orbital plays a minor role (P_B = 0.35). This means that the U5f–F2s/2p overlap populations for the nonrelativistic case are approximately one-third of those for the relativistic one. The relativistic U5f AO is expanded in comparison with the nonrelativistic one and can overlap much more with the F2s/2p AOs. The antibonding interactions are attributed to the U6s/6p–F2s/2p interactions. In the nonrelativistic calculations, the P_B values of the U6s–F2s/2p and U6p–F2s/2p antibonding interactions are –0.45 and –1.20, whereas they are –0.29 and –1.16 in the relativistic case. The large decrease in the U6s–F2s/2p antibonding interactions is due to the U6s orbital contraction. Both relativistic contraction of the U6s AO and relativistic expansion of the U5f AO increase

the bond overlap populations. This increase in the bond strength has also been discussed for UF_6 in details [13]. Consequently, the relativistic calculation becomes important for investigating the electronic structure and chemical bonding of UF_5, though there has been a report on nonrelativistic Xα scattered-wave calculations [51]. The relativistic calculation demonstrates that not only the U6d AO but also the U5f one effectively contributes to the U–F bonding.

Table 4. Comparison of orbital populations, effective charges of U and F atoms, and bond overlap populations between C_{4v}, D_{3h}, and C_{2v} geometries along with those of the previous work [ref. 5 corresponding to ref. 50 cited in this review].

		orbital population					
		present study				previous study[5]	
atom	orbital	C_{4v}[a]	D_{3h}[b]	C_{2v}[c]		C_{4v}[d]	D_{3h}[b]
U	$5f_{5/2}$	1.81	1.86	1.82	f	1.97	1.94
	$5f_{7/2}$	1.24	1.18	1.26			
	$6s_{1/2}$	1.99	1.99	1.99	s	2.18	2.18
	$6p_{1/2}$	1.98	1.98	1.98	p	6.31	6.30
	$6p_{3/2}$	3.90	3.90	3.89			
	$6d_{3/2}$	0.67	0.69	0.66	d	1.18	1.20
	$6d_{5/2}$	0.90	0.91	0.89			
	$7s_{1/2}$	0.08	0.08	0.09			
	$7p_{1/2}$	0.10	0.10	0.09			
	$7p_{3/2}$	0.16	0.16	0.16			
eff charge		1.16	1.15	1.17		2.36	2.38
F_{eq}	$2s_{1/2}$	1.93	1.93	1.93	s	1.94	1.93
	$2p_{1/2}$	1.78	1.78	1.78	p	5.54	5.55
	$2p_{3/2}$	3.52	3.53	3.52			
eff charge		−0.23	−0.24	−0.24		−0.48	−0.46
F_{ax}	$2s_{1/2}$	1.92	1.93	1.93	s	1.94	1.94
	$2p_{1/2}$	1.78	1.77	1.78	p	5.54	5.53
	$2p_{3/2}$	3.53	3.51	3.52			
eff charge		-0.23	−0.21	−0.22		−0.48	−0.47
bond overlap population		1.79	1.77	1.79			

[a] $U–F_{ax} = 2.00$ Å, $U–F_{eq} = 2.02$ Å, $F_{ax}–U–F_{eq} = 101°$.[1] [b] $U–F_{ax} = 1.99$ Å, $U–F_{eq} = 2.02$ Å, $F_{ax}–U–F_{eq} = 90°$.[5] [c] $U–F_{ax} = 2.00$ Å, $U–F_{eq} = 2.02$ Å, $F_{ax}–U–F_{eq} = 90°$, $F_{eq}–U–F_{eq} = 101°$. (intermediate between C_{4v} and D_{3h}). [d] $U–F_{ax} = 2.00$ Å, $U–F_{eq} = 2.00$ Å, $F_{ax}–U–F_{eq} = 100°$.[5]

We next examined the electronic structure of UF_5 with the C_{2v} intermediate structure (two $F_{eq}–U–F_{eq}$ bond angles in the D_{3h} structure are reduced from 120 to 101°) between the C_{4v} and D_{3h} structures. Table 4 shows the results for the intermediate geometry along with those for the C_{4v} and D_{3h} structures. The effective charges on the equatorial and axial fluorine atoms are –0.24 and –0.22, respectively, and that on the uranium atom is +1.17. The bond overlap population of the C_{2v} intermediate structure is +1.79. These values are almost equal to those of the C_{4v} and D_{3h} structures. In addition, the one-electron energies and orbital components for the C_{2v} geometry are similar to those for the other structures. These findings suggest that the energy barrier between the C_{4v} and D_{3h} structures is very small and both structures are

interconvertible. Consequently, the results of the present study agree with the previous theoretical result [50] that the gaseous UF_5 monomer fluctuates between C_{4v} and D_{3h} structures. Unfortunately, it is difficult to confirm this theoretical prediction experimentally at this stage.

On the basis of the above results obtained using the bond overlap population analysis, we attempt to interpret the origin of the fluxional structure of the UF_5 monomer qualitatively. Studies on the difference in theoretical energies (ΔE) between the C_{4v} and D_{3h} structures for other pentafluorides such as SF_5 [52,53] and PF_5 [54, 55] have been reported. The ΔE values for SF_5 and PF_5 were estimated to be 0.90–1.57 and 0.18–0.21 eV, respectively. On the other hand, the ΔE for UF_5 is reported to be 0.04 eV [50]. Thus, UF_5 is considered to be more fluxional between the two structures than the other pentafluorides. This fluxtional structure originates from the fact that the U5f AO plays a major role in the U–F bonding and has wide angular distributions resulting in the flexibility of the bond angle in hybridization with the U6d AO. This cannot be explained in the framework of nonrelativistic calculations, because the U5f electrons play a minor role in the chemical bonding in the nonrelativistic case. Finally, we evaluated the first ionization potential (IP) of the UF_5 monomer with the C_{4v} experimental structure using Slater's transition method [56] and obtained an IP value of 9.8 eV, which was in reasonable agreement with the experimental value of 11.29 eV [57].

4. Electronic Structure of Uranium Complexes

Uranyl nitrates play an important role in the nuclear fuel cycle. Information on the electronic structure of various kinds of uranyl nitrate complexes in solution becomes very important to understand their stability and to design useful ligands. A typical form of uranyl nitrate in nitric acid solution is $UO_2(NO_3)_2$-$2H_2O$, where the UO_2 species is surrounded by four oxygen atoms of the two bidentate nitrate groups and two oxygen atoms of the two equivalent water molecules, as shown in Fig. 7.

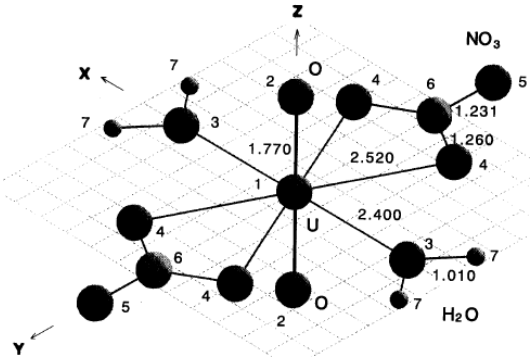


Figure 7. Schematic illustration of the structure of uranyl nitrate [58, 59]. Interatomic distances are shown in Ångströms.

Table 5. Atomic orbital components and XPS intensities for valence states of $UO_2(NO_3)_2$-$2H_2O$ with D_{2h} symmetry.

Orbital	Energy/ eV	Intensity	U			O(O=U)		O(O–H_2)		O(U–O_2NO)		O(O–NO_2)		N		(7) H
			5f (245)	6p (58.8)	6d (34.1)	2s (35.2)	2p (5.46)	2s (35.2)	2p (5.46)	2s (35.2)	2p (5.46)	2s (35.2)	2p (5.46)	2s (21.7)	2p (2.50)	1s (0.20)
48γ5u	−6.6	26.4	0.09								0.29		0.60			
47γ5g	−6.7	7.1			0.06						0.25		0.69			
47γ5u	−7.1	23.9	0.07	0.02			0.07				0.32		0.51			
46γ5g	−7.1	5.4					0.06				0.36		0.58			
45γ5u	−7.5	5.3									0.97					
46γ5u	−7.7	16.5	0.05								0.95					
45γ5u	−7.7	10.2	0.02								0.67		0.26			
44γ5u	−7.8	5.3									0.77		0.21			
44γ5u	−7.9	38.9	0.13	0.04			0.12		0.07		0.50		0.12			
43γ5u	−8.2	57.5	0.21	0.04			0.21		0.18		0.28		0.06			
43γ5u	−8.5	5.4			0.02		0.29		0.59							
42γ5g	−8.7	6.2				0.04	0.60				0.29					
42γ5u	−9.3	53.5	0.20	0.02			0.45		0.26		0.05					
41γ5u	−9.4	4.9		0.01			0.27		0.42		0.05		0.02			
41γ5u	−9.4	60.1		0.21	0.09		0.29		0.01		0.43		0.09			
40γ5u	−9.7	78.4	0.31				0.59		0.06		0.02					
40γ5g	−9.8	12.2			0.24		0.69						0.03			
39γ5g	−10.4	12.3			0.24		0.47		0.26		0.03					
39γ5u	−11.5	29.4	0.09	0.01			0.04	0.08	0.62							0.12
38γ5g	−12.5	10.7			0.06			0.05	0.48	0.05	0.10	0.04	0.06		0.04	0.09
38γ5g	−12.6	13.8							0.01	0.05	0.18	0.25	0.33		0.16	
37γ5g	−12.8	13.5			0.04			0.01	0.17	0.02	0.12	0.22	0.27		0.11	0.02
36γ5g	−13.3	10.5			0.04				0.16	0.16	0.33		0.04		0.16	0.10
37γ5u	−13.5	16.7	0.02							0.22	0.47		0.05		0.21	
36γ5g	−13.8	3.7									0.28		0.11		0.61	
35γ5g	−13.8	3.6									0.28		0.11		0.61	
35γ5u	−14.3	8.5							0.48	0.08	0.04	0.05	0.03	0.04		0.28
34γ5g	−14.9	5.7			0.02				0.48	0.04	0.14				0.05	0.27
34γ5u	−15.5	19.1	0.01	0.02					0.14	0.28	0.23	0.07	0.02	0.09		0.08
33γ5g	−15.5	21.7			0.02				0.02	0.33	0.28	0.12	0.04	0.13		
33γ5u	−17.2	43.7	0.03	0.31		0.50	0.08		0.01		0.01					
32γ5u	−22.1	51.7		0.85			0.02	0.02	0.03		0.02	0.01				
32γ5c	−23.9	34.6			0.13	0.82	0.02									
31γ5u	−25.7	26.2		0.06		0.03				0.55	0.03	0.05			0.28	
31γ5g	−25.8	24.3								0.66	0.03				0.29	
30γ5u	−25.9	28.7		0.12		0.05		0.20	0.02	0.19	0.01	0.17	0.01		0.19	0.05
30γ5g	−26.1	22.5						0.04		0.19	0.02	0.39	0.04		0.33	
29γ5u	−26.5	29.3		0.12		0.03		0.34	0.01	0.08	0.01	0.17	0.02		0.14	0.09
29γ5g	−26.5	27.9			0.01			0.76	0.02			0.02			0.01	0.17
28γ5u	−27.5	44.9	0.01	0.44		0.17	0.03	0.24		0.03		0.02			0.02	0.06
28γ5g	−31.5	25.5								0.30	0.09	0.12	0.04	0.47		
27γ5u	−31.6	23.9		0.02						0.30	0.08	0.11	0.04	0.47		
26γ5u	−33.4	51.3		0.77		0.15	0.05			0.01						

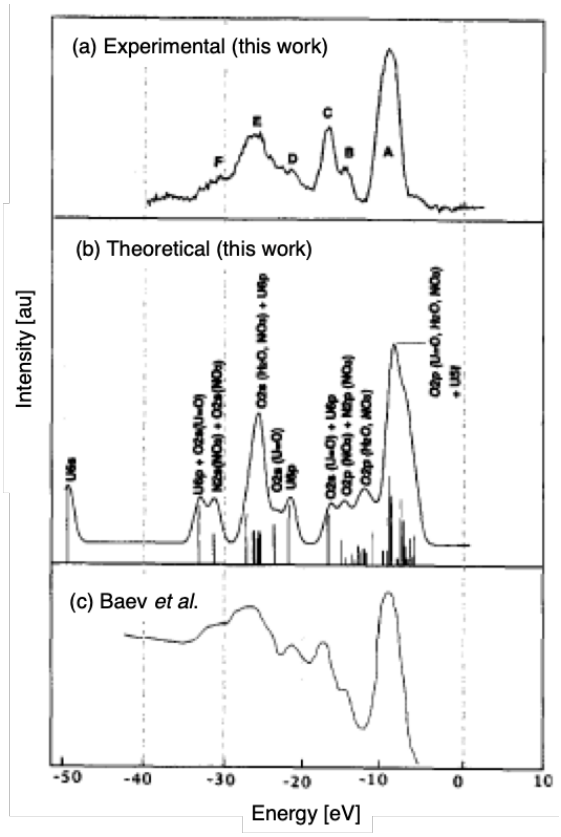


Figure 8. Experimental (a) and theoretical (b) XPS spectra of uranyl nitrate, $UO_2(NO_3)_2$-$2H_2O$, along with the experimental spectrum (c) reported by Baev *et al.* [58].

Hirata *et al.* investigated experimental XPS spectrum by comparison with theoretical one [18]. Table 5 summarizes AO components and XPS intensities for the valence states of $UO_2(NO_3)_2$-$2H_2O$, and Figure 8 shows the experimental (a) and theoretical (b) XPS spectra of uranyl nitrate, $UO_2(NO_3)_2$-$2H_2O$, along with the experimental spectrum (c) reported previously [58]. In this figure, the $48\gamma_{5u}$ HOMO was shifted so as to be at the valence-band edge of the experimental spectrum (a). The theoretical spectrum was obtained by replacing each calculated MO level with a Gaussian function whose FWHM is set to 1.2 eV based on the experimental spectrum (a). It can be seen from Fig. 8 that the theoretical spectrum (b) is generally in good agreement with the experimental spectra.

The highest peak A consists of the $48\gamma_{5u}$ to $39\gamma_{5g}$ MOs. The MOs of $48\gamma_{5u}$ to $43\gamma_{5u}$ have the O2p AO of the nitrate group ($-NO_3$) as a main component, whereas those of $43\gamma_{5g}$ to $39\gamma_{5g}$ contain the U5f, U6d and O2p AOs of the uranyl oxygen (U=O). The peak B consists of the $39\gamma_{5u}$ to $33\gamma_{5g}$ MOs which are mainly constructed of the O2s, 2p and N2p AOs of the nitrate group. Some of these MOs may be included in peak C. The peak C corresponds to the $33\gamma_{5u}$ orbital containing the U6p (31%) and O2s (50%) AOs of the UO_2 group. The shoulder D at about -22 eV corresponds to the $32\gamma_{5u}$ orbital containing the U6p AO as a

main contribution. The broad peak E in the range –24 to –28 eV consists of the $32\gamma_{5g}$ to $28\gamma 5u$ MOs which contain the U6p and ligand O2s AOs. Finally, the weak peak F in the range –31 to –33 eV on the lower energy side of the peak E consists of the $28\gamma_{5g}$, $27\gamma_{5u}$ and $26\gamma_{5u}$ MOs which contain U6p, O2s and N2s AOs of the nitrate group. The calculated spectrum around the peak B has a different shape from the experimental one, although the whole theoretical spectrum except this part is in good agreement with the experimental ones. The calculated energies for the peaks B and C are slightly higher than the experimental ones.

In a similar manner, Hirata *et al.* succeeded in assigning the experimental XPS spectrum of actinyl nitrate-phosphate complexes [19].

5. Uranium carbide, uranium metal, and uranium alloys

Kurihara *et al.* applied DV-DS method to uranium compounds such as uranium carbide, uranium metal, and uranium alloys [22–27].

5.1. Uranium carbide

For a cluster model of uranium carbides (UC) with a NaCl-type structure, we employed neutral UC_6, CU_6, and CU_6C_{18} cluster models with Oh symmetry and with a U-C bond length of 248.1 pm taken from the experimental results [59], as shown in Fig. 9.

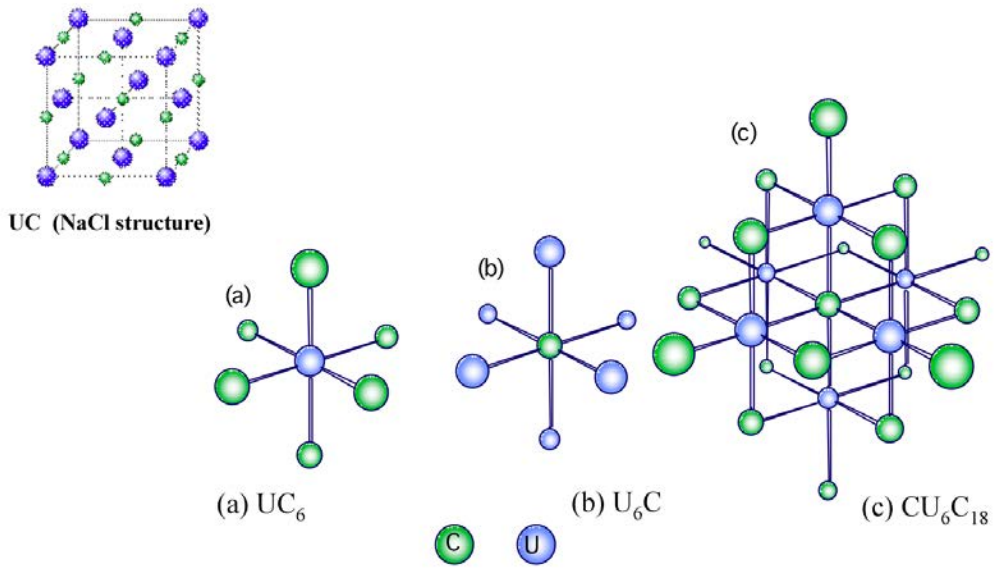


Figure 9. Schematic illustration of cluster models for UC with a NaCl-type crystal structure: (a) UC_6, (b) CU_6, and (c) CU_6C_{18} [Ref. 22].

In case of the CU_6C_{18} cluster, the CU_6 cluster was embedded with eighteen carbon atoms. Since the spin function is included in the Dirac equation explicitly, the Oh symmetry reduces to the Oh* double group [60]. Symmetry orbitals for the irreducible representations of Oh* symmetry were constructed from AOs by the projection operator method [61]. All the calculations were performed with the Slater exchange parameter α of 0.7. Computational details have been described elsewhere [22].

Figure 10 shows the experimental valence XPS spectra of UC [62] (a) and theoretical spectra for the UC_6 (b), CU_6 (c), and CU_6C_{18} (d) cluster models shown in Fig. 9, along with the partial density-of-states (pDOS) of the U5f and U6d AOs (e) and of the C2s and C2p AOs (f). As shown in Fig. 10a, UC has the intense peak "1" at the Fermi level (E_F), the shoulder peak "2" at around –2 eV, and the broad weak peak "3" at around –10 eV. We next compared theoretical spectra [Figs. 10b–10d] with the experimental result. As shown in Fig. 10b, the UC_6 cluster model well reproduced both relative intensity and position (binding energy) for the peaks "1" and "3", but the shoulder peak "2" unfortunately seemed not to be reproduced. On the other hand, the CU_6 cluster model showed a peak corresponding to the peak "2" besides the peaks "1" and "3", but it was completely separated (not a shoulder peak) from the peak "1". Accordingly, it is found that the CU_6 cluster model reproduces the experimental spectra better than the UC_6 cluster model. When the CU_6 cluster is surrounded with eighteen C atoms, a CU_6C_{18} embedded cluster model is expected to reproduce the experimental spectra better than the CU_6 cluster. Comparison between Figs. 10a and 10d indicates that the theoretical spectra well reproduce the whole experimental one.

To assign the three peaks shown in Fig. 10a, we next examined the pDOS based on the results of the CU_6C_{18} embedded cluster model. Figures 10e shows the pDOS of the U5f (dashed line) and U6d (solid line) AOs, whereas Figure 10f shows that of the C2s (solid line) and C2p (dashed line) AOs. Comparison between Figs. 10a and 10e-f indicates that the intense peak "1" is mainly attributed to the U5f AO which has a large photo-ionisation cross-section and the shoulder peak "2" is attributed to the U6d–C2p AOs, whereas the broad weak peak "3" is mainly attributed to the C2s AO.

In previous reports by the other groups, Schadler *et al* reported that the intense peak "1" was due to the U5f–U6d bands, while the shoulder "2" due to the U6d–C2p band [63]. On the other hand, Ejima *et al* concluded that a small amount of the U5d component contributes to the shoulder "2". However, because the $U5d_{5/2}$ and $U5d_{3/2}$ AOs are respectively located at –91 eV and –99 eV, the U5d components can be considered to play a minor role for the shoulder "2". In fact, the present calculations show that the U5d components have no contribution to the valence electronic structure of UC.

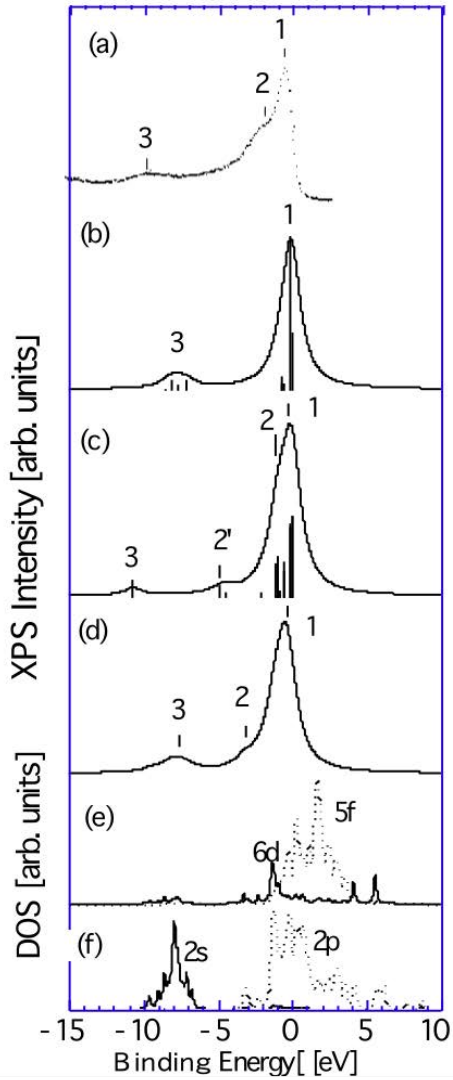


Figure 10. Theoretical and experimental valence x-ray photoelectron spectra for UC: (a) experiment [62] and theoretical spectra obtained using (b) UC_6, (c) CU_6, and (d) CU_6C_{18} cluster models, along with partial density-of-states (pDOS) for (e) the U5f (dashed line) and U6d (solid line) AOs and (f) the C2s (solid line) and C2p (dashed line) AOs.

5.2. Uranium metal

Figure 11 shows (a) the unit cell of α-U metal crystal with an orthorhombic structure and (b) the U_9 cluster model with the central U atom (1) surrounded by eight U atoms (2–8). The geometry of the present cluster has a C_{2v} symmetry with the U–U bond length of 5.219 au between (1) and (2), 5.389 au between (1) and (4), and 6.165 au between (1) and (6) and between (1) and (8) on the basis of the experimental results of α-U metal [64]. Symmetry orbitals for the irreducible representations of C_{2v}[*]

symmetry were constructed from AOs by the projection operator method [61]. All the calculations were carried out under the same conditions as for UC, as described in the previous section.

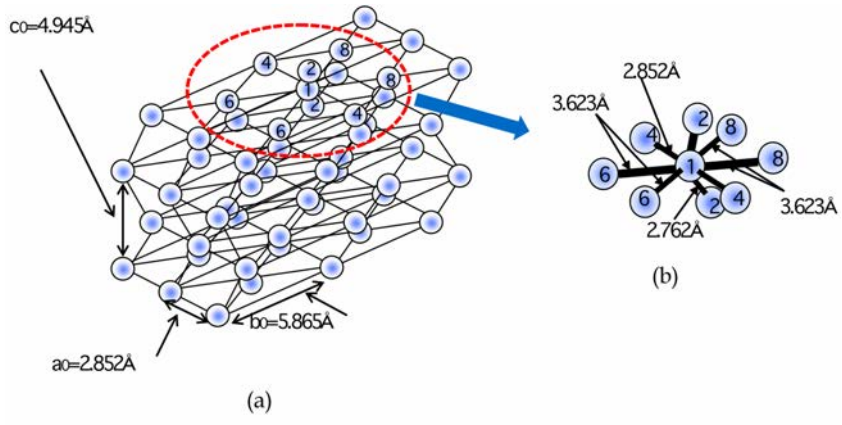


Figure 11. Schematic illustration of α-U metal: (a) the orthorhombic structure of α-U metal and (b) a U_9 cluster model used as the minimum unit of α-U crystal structure [23].

Figure 12 shows (a) the experimental [65] and theoretical x-ray photoelectron spectra obtained using the U_9 cluster model [23] for α-U metal, (b) the pDOS of U valence AOs, and (c) the magnified pDOS in the vicinity of E_F. As shown in Fig. 12a, it is interesting to note that the theoretical spectra well reproduced the experimental one of α-U metal, in spite of using the minimum U_9 cluster model shown in Fig. 12. By comparison between Figs. 12a and 12b, it is clearly found that the peaks "B" and "C" are only attributed to the U6$p_{3/2}$ and U6$p_{1/2}$ AOs, respectively. In a similar manner, the intense peak "A" appearing at E_F is mainly attributed to the U5$f_{7/2}$ and U5$f_{5/2}$ AOs. As shown in Fig. 12c, since the other valence AOs such as the U6d, U7s, and U7p are located around E_F, they contribute to the peak "A" to some extent. However, because their photo-ionisation cross-sections are much smaller than that of the U5f AOs, they are considered to have minor contributions.

In the previous band calculations [66], they compared the DOS structures with the experimental spectra, and discussed the assignment of each peak qualitatively. On the contrary, the present method can calculate XPS intensity of individual MOs for the cluster model used as the minimum unit of α-U metal. Thus, we have quantitatively obtained the valence XPS spectra, together with pDOS of individual AOs contained in each MOs. This enables us to assign individual peaks satisfactorily.

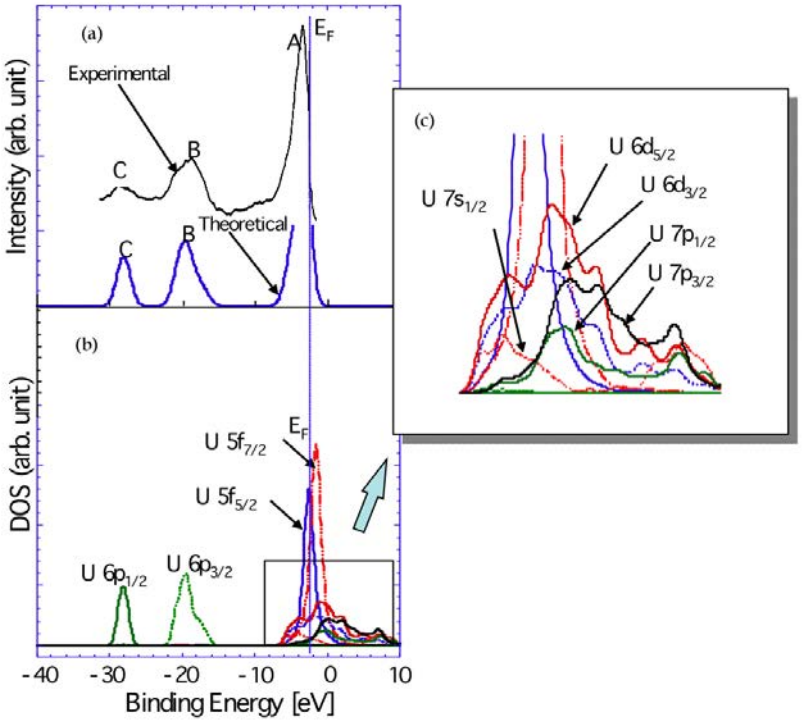


Figure 12. (a) Experimental [65] and theoretical spectra, (b) partial density-of-states (pDOS) of U valence AOs and (c) magnified pDOS in the vicinity of E_F [23].

5.3. Uranium alloys

To use advanced nuclear fuels practically, it is critical to understand the dissolution process of transition-metal (TM) atoms into γ-U on the basis of their phase diagrams [67, 68]. The alloying behavior of U compounds has been hitherto theoretically investigated by considering the relative stabilities of electronic configurations [69, 70] and the thermodynamics [71]. Hume-Rothery *et al.* focused on the metallic radius of TM elements as a parameter for understanding their alloying behavior [72]. According to their empirical findings, when the difference in the metallic radius between solute and solvent atoms is less than 15%, TM elements are very soluble to each other. Figure 13 shows the correlation between U/TM radius and the maximum solid solubility (MSS) of TM into γ-U. Here, the dashed line denotes the metal radius smaller by 15% than that of γ-U [73, 74].

This rule seems to explain MSS for 3d-TM/γ-U alloys, but cannot explain MSS for 4d- and 5d-TM/γ-U alloys. Furthermore, Buzzard pointed out that the miscibility of TMs into γ-U depends on compatibility factors considering ionic radius, electron negativity, and the number of d-electrons [69, 70]. However, because many empirical parameters should be determined, this evaluation process of their alloying behaviors is not applicable to other actinide alloy systems. On the other hand, Ogawa *et al*. investigated

the alloying behavior by using the ChemSage program [75], and concluded that the difference in the excess free energy (ΔG^{E}) of the U/Mo, U/rhodium (Rh), and U/palladium (Pd) alloying systems may be due to the contribution of the U6d–Pd4d orbital interactions [71]. Although the interactions indeed play an important role in their alloying behaviors, it is necessary to clarify what interactions between γ-U and TMs contribute to the alloying behavior quantitatively in order to satisfactorily understand the alloying behavior of the 3d, 4d and 5d TMs into γ-U solid.

To understand the dissolution of these TM elements into solid γ-U in addition to obtain the phase diagram or phase equilibria, it is indispensable to determine which electronic terms contribute to the thermodynamic properties of U alloys by comparing DFT calculations with experimental results.

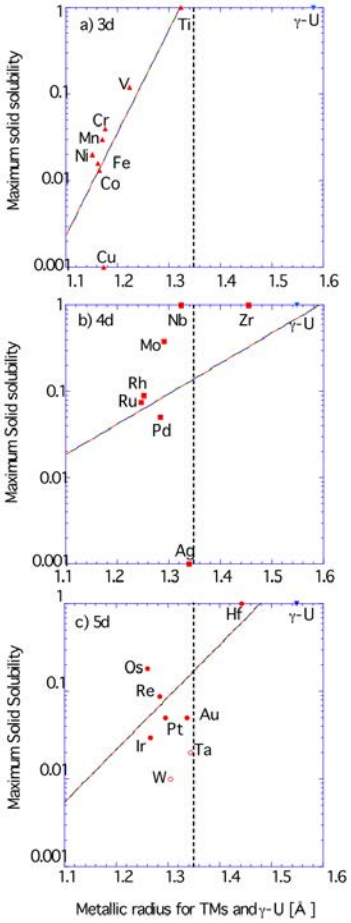


Figure 13. The correlation between the metallic radius of TMs and the maximum solid solubility (MSS) for γ-U alloyed with (a) 3d TMs, (b) 4d TMs, and (c) 5d TMs [Ref. 25].

We have investigated the alloying behavior of 3d-, 4d- and 5d-TMs into γ-U, using the DV-DS MO method which takes into account fully relativistic effects including the spin-orbit coupling, and found that

the maximum solid solubility (MSS) of TMs into γ-U is exponentially proportional to both the d-orbital energy of TM (Md) and the orbital overlap population (OOP) between TMd and U6d AOs.

Figure 14 shows schematic representation of a cluster model of γ-U alloyed with TMs. As shown in Fig. 14, the central U atom, U(1), was substituted with TM atoms. To compare the difference in the electronic structure among the γ-U/TM alloys, the MO energy level structure and chemical bonding of the alloys were examined [24]. In the present works, the lattice relaxation in association with TM element substitution to γ-U solid was ignored, because the Md and OOP may not be affected significantly by the lattice relaxation [76–78]. The lattice constant of γ-U crystal was taken from the experimental result of 6.659 au [64]. All the calculations were carried out self-consistently under the same conditions as for UC and α-U, as described in the previous sections.

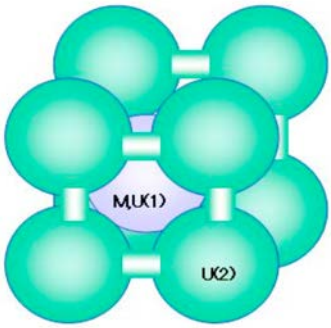


Figure 14. Schematic illustration of TM/γ-U alloy cluster model: the central U atom (1) replaced with TM atom [24].

Figure 15 schematically illustrates the stabilization energy (ΔE) caused by the U6d–TMd orbital interactions from a viewpoint of molecular orbital theory (top) and the correlation between maximum solid solubility (MSS) and ΔE or the U6d–TMd energy difference (bottom). Here, α_U and α_{TM} respectively denote the U6d and TMd energies, and α_U is equal to or greater than α_{TM} ($\alpha_U \geq \alpha_{TM}$).

ΔE can be expressed as $\Delta E = |\beta|\{(x^2 + 1)^{1/2} - x\}$ [79]. Here, $x = (\alpha_U - \alpha_{TM})/2|\beta| \geq 0$, and β denotes the resonance integral between U6d and TMd AOs. Accordingly, ΔE decreases monotonically with increasing x, and becomes the minimum (near equal to zero) when $(\alpha_U - \alpha_{TM})$ is much larger than unity (>>1). On the other hand, ΔE has the maximum value of $|\beta|$ when $(\alpha_U - \alpha_{TM})$ is zero. Consequently, a larger MSS for γ-U/TM alloys is obtained at a lower value of $(\alpha_U - \alpha_{TM})$ (corresponding to a larger ΔE), whereas a small MSS is obtained at a larger value of $(\alpha_U - \alpha_{TM})$ (corresponding to a smaller ΔE). Consequently, it can be concluded that the magnitude of ΔE caused by the TMd–U6d orbital interactions plays a key role of determining the magnitude of MSS.

As described in Ref. 26, MSS exhibits an exponential dependence on both Md [in other words, the U6d–TMd energy difference, ($\alpha_U - \alpha_{TM}$)] and the U6d–TMd OOP. In the present work, we employed the cluster model (see Fig. 14) for γ-U/TM alloys by substituting the central U atom with TM atoms. The following equilibrium has been considered based on the cluster model, $U_9 + TM \Leftrightarrow U_8TM + U$. Here, TM denotes a TM atom in the TM bulk phase, while U_9/U_8TM and U respectively denote a cluster and a U atom in the γ-U bulk phase. As the equilibrium constant (K), the concentration of U_8TM increases, thus increasing MSS. On the other hand, as K decreases, the U_8TM concentration correspondingly decreases, thus reducing MSS. Accordingly, MSS is proportional to K. The MSS and K can then be written as, MSS $\propto K = Ae^{-\Delta G/RT}$, where A is a constant, ΔG denotes the Gibbs free energy difference before and after the substitution, R is the gas constant, and T is the absolute temperature. Since the lattice relaxation on substitution is negligible, the entropy is constant ($\Delta S = 0$) in the present substitution model. Thus, ΔG is equal to the enthalpy difference (ΔH) before and after the substitution. Accordingly, MSS $\propto K = Ae^{-\Delta G/RT} = Ae^{-\Delta H/RT}$. Since ΔH includes ΔE due to the TMd–U6d orbital interactions, the following relationship is obtained: MSS $\propto K = Ae^{-\Delta G/RT} = Ae^{-\Delta H/RT} \propto e^{\Delta E/RT}$. As described above, ΔE is disproportional to ($\alpha_U - \alpha_{TM}$) and increases with $|\beta|$ which is proportional to OOP. Consequently, the MSS depends exponentially on both Md and the OOP.

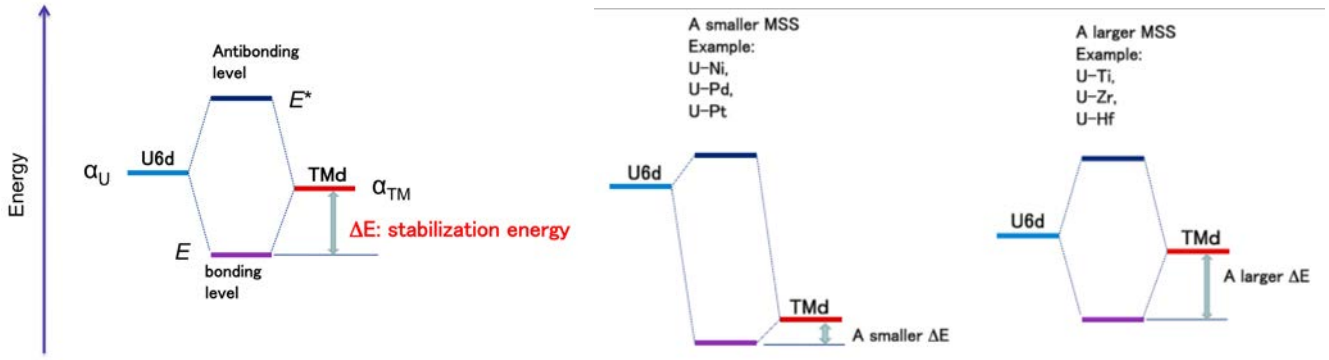


Figure 15. Schematic illustration of the TMd–U6d orbital interactions based on molecular orbital theory (left) and of the correlation between MSS and the stabilization energy (ΔE) caused by their orbital interactions (right) [26].

In the above discussion, Md and OOP can be regarded as a good parameter to determine the magnitude of MSS. Then, we next made the OOP–Md map for γ-U/TM alloys, as shown in Fig. 16. Interestingly, γ-U/TM alloys with a smaller MSS appear in the lower-left region of the map, whereas those with a higher MSS in an upper right hand. This is a universal tendency with disregard to 3d/4d/5d TM elements.

Consequently, the OOP–Md map could be useful for designing γ-U/TM alloys. We believe that the present findings can be used for not only the γ-U/TM alloy system but also other actinide alloys used as nuclear fuels for advanced reactors.

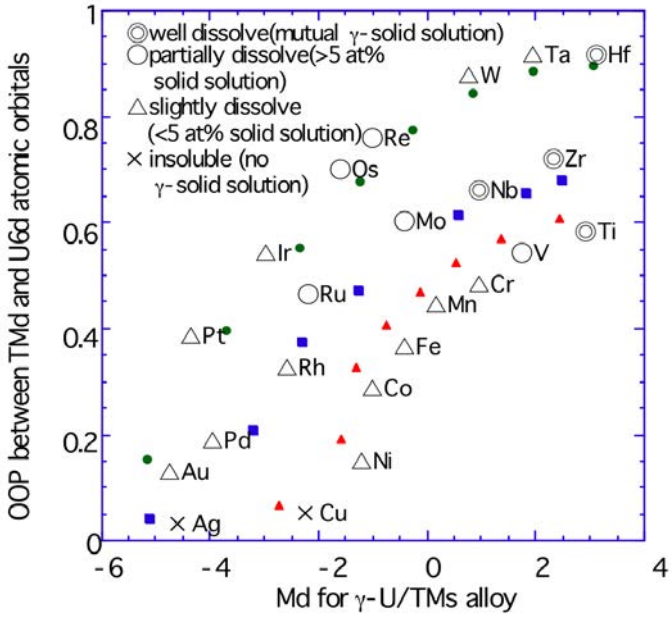


Figure 16. OOP vs. Md plot of γ-U/TM alloys [26].

6. Carbon nanomaterials: Electronic structure of C_{120} isomers

Onoe *et al*. have investigated the electron-beam (EB) induced polymerization of C_{60} film [80–90], and found that one-dimensional (1D) peanut-shaped C_{60} polymer is formed [91, 92] and exhibits physical properties arising from 1D metal [93–102].

The 1D polymer is fascinating from a viewpoint of topology, because it has both positive and negative Gaussian curvatures (k) in the waist region of the cross-linkage between adjacent C_{60} molecules (see Figure 17). When π-electron conjugated carbon isomers are classified with Gaussian curvatures, this peanut-shaped polymer can be regarded as a new topological carbon (see Table 6), which is different from graphite ($k = 0$), C_{60} ($k > 0$), CNTs ($k = 0$ at body, $k > 0$ at both edges if they have a capped structure), and hypothetical Mackay crystals ($k < 0$). Here, Gaussian curvature of a smooth surface in three-dimensional Euclidean space is defined to be the product of the two principal curvatures, κ_{min} and κ_{max}, at a given point: $k = \kappa_{min}\kappa_{max}$. Here, κ_{min} and κ_{max} denote the minimum and maximum normal curvatures at that point, respectively. As shown in Fig. 17, the peanut-shaped structure has two features: one is the positive

and negative Gaussian curvatures lined alternatively and periodically in the 1D chain, and the other is the waist region consisting of multi-membered rings, especially 7- and/or 8-membered ring.

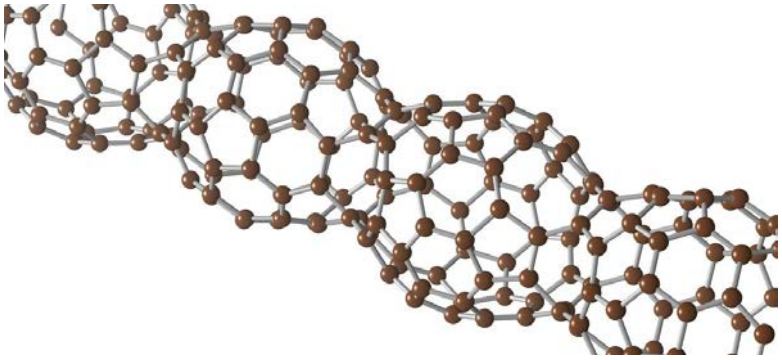
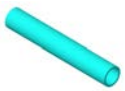
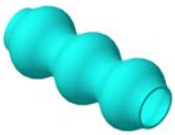


Figure 17. Schematic representation of 1D peanut-shaped C_{60} polymers [28].

Table 6. Classification of π-electron conjugated carbon allotropes based on Gaussian curvature. Here, "+" and "–" indicate positive and negative signs, respectively.

Nanocarbon materials	Gaussian curvature k	Geometrical shape
graphene	0	
fullerenes	+	
nanotubes	0（body），+ （cap）	
Mackay crystal (hypothetical)	–	
1D peanut-shaped polymer	+, –	

One has a next question how which and/or both of the two features contribute to the metallic properties of the 1D peanut-shaped polymer. The purpose of the present study is to understand the role of the multi-membered rings in the waist region for the metallic properties at the first stage in order to answer the question. To clarify the role of the multi-membered rings, we have examined the electronic structure

of all the C_{120} stable isomers (see Figure 18) derived from the general Stone-Wales (GSW) rearrangement [103], because they can be regarded as a minimum unit of 1D C_{60} polymer candidates.

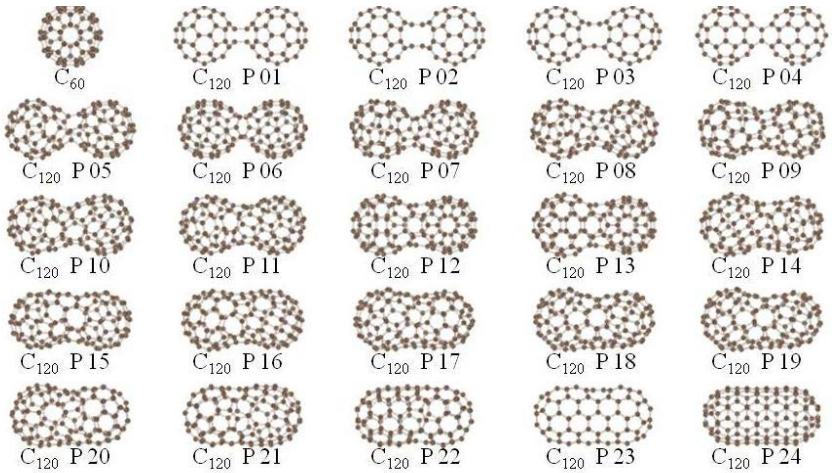


Figure 18. Schematic illustration of the stable C_{120} isomers derived from the general Stone-Wales rearrangement. Where, *n*-th C_{120} isomer is denoted as P*n* [28].

There have been some reports dealing theoretically with the electronic properties of CNTs with multi-membered rings [104–106]. One of which introduced several multi-membered rings to CNTs by removing carbon atoms from 6-membered rings of CNTs [104]. However, they focused on the effect of vacancies on the electronic structure of CNTs rather than that of multi-membered rings. In addition, the multi-membered rings thus formed are unstable because of many dangling bonds, which are quite different from the multi-membered rings (with no dangling bonds) in the waist region of the 1D peanut-shaped polymer. On the other hand, the others of which investigated the connection between CNTs with different diameters by introducing 5- and 7-membered rings into CNTs [105, 106], and found that the two multi-membered rings affect the electronic properties of CNTs. This suggests that the 7- and 8-membered rings will affect the electronic properties of the 1D peanut-shaped polymer.

Although there have been hitherto some theoretical reports on the electronic state of 1D peanut-shaped C_{120} isomers [81, 83, 107, 108], no attempts to examine the electronic properties of all the C_{120} stable isomers, which are derived from GSW rearrangement, have been made until now.

To examine how the multi-membered rings in the waist region contribute to the energy gap of individual C_{120} isomers, we employed the DV-Xα method based on local density-functional approximation [3]. Because the DV-Xα method uses numerical AOs optimized in a molecular potential, it is easy to estimate the contribution of individual membered rings to the energy gap, effective charges, and MOs.

We examined all the C_{120} stable isomers shown in Fig. 18. Here, *n*th C_{120} isomer is expressed as P*n*. For example, the initial dumbbell-shaped C_{120} isomer is denoted as P1, whereas the C_{120} nanotube (the final state) as P24. All the C_{120} isomers were calculated by the DV-Xα MO method with the Slater exchange parameter (α) of 0.7 for all carbon atoms and with 60000 DV sampling points, which provides a precision of less than 0.1 eV for the valence electron energy eigenvalues [3]. We used the basis functions up to the 2p orbitals. The calculations were carried out self-consistently until the difference in orbital populations between the initial and final states of the iteration was less than 0.01. The computational details of the present method have been described elsewhere [28]. For the effective charges of all the C_{120} isomer, the precision of polarization degree was less than 0.05 electrons. We visualized the highest occupied MO (HOMO) and the lowest unoccupied MO (LUMO) wavefunctions and effective charges for all the C_{120} isomers, using the VESTA program developed by Izumi *et al* [109].

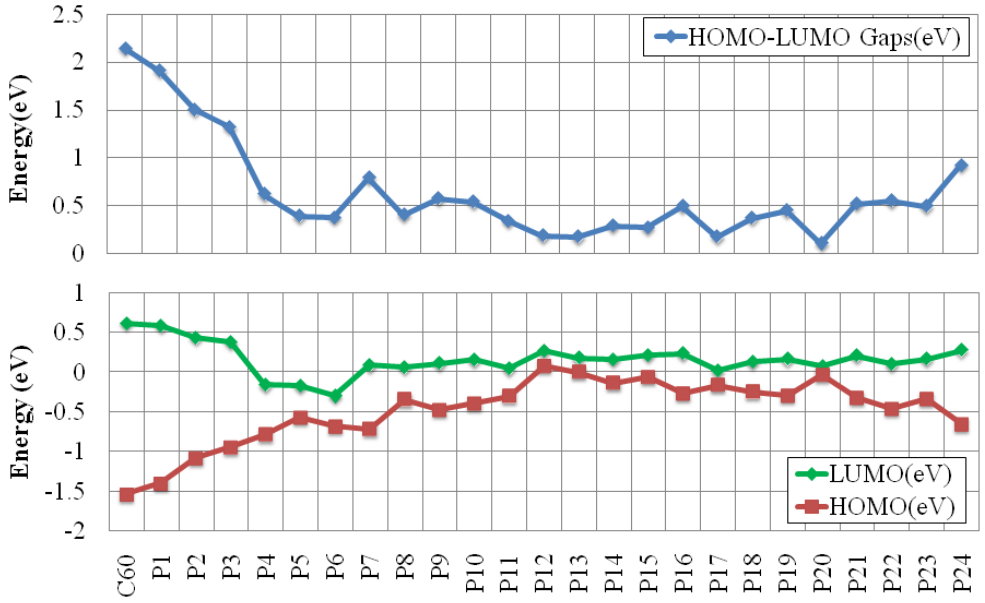


Figure 19. The HOMO-LUMO gap (top) and the energy level of the HOMO and LUMO (bottom) for each C_{120} isomer [28].

Figure 19 shows the comparison of the HOMO-LUMO gap among all the C_{120} isomers. The HOMO-LUMO gap of C_{60} was estimated to be 2.1 eV, which is somewhat larger than that of 1.6–1.8 eV obtained experimentally [110]. This discrepancy may be due to the ignorance of the orbital relaxation effects [56], the use of the Xα potential and/or of the minimum basis sets [3]. However, the difference in the energy gap value between the DV-Xα and experimental results is a systematic error and remains almost unchanged within 0.5 eV for all the isomers. This allows us to discuss the structural dependence of

the HOMO-LUMO gap and the role of multi-membered rings for each isomer. As shown in Fig. 19, the HOMO-LUMO gap of the C_{120} isomer decreases noticeably to 0.4 eV in going from C_{60} to P6 isomer, and subsequently fluctuates at around 0.3 eV up to P23 isomer and finally increases to 0.9 eV for P24 isomer. Among all the isomers, P20 isomer has the smallest HOMO-LUMO gap of 0.1 eV.

Table 7 summarizes the number of the 7- and 8-membered rings contained in each isomer. It is found from Fig. 19 and Table 7 that the C_{120} isomer with an 8-membered ring tends to have a relatively lager HOMO-LUMO gap than for one without the ring.

Table 7. The number of 7- and 8-membered rings included in each C_{120} isomer.

Isomer	P1	P2	P3	P4	P5	P6	P7	P8	P9	P10	P11	P12
7-Membered rings	0	0	0	0	2	4	4	5	5	6	6	7
8-Membered rings	0	0	0	0	0	1	1	0	1	1	0	0
Isomer	P13	P14	P15	P16	P17	P18	P19	P20	P21	P22	P23	P24
7-Membered rings	5	5	6	5	5	3	3	4	4	4	2	0
8-Membered rings	0	0	0	0	0	0	0	0	0	0	0	0

Table 8. The contribution of 7- and 8-membered rings to the HOMO and LUMO for each C_{120} isomer, along with their HOMO-LUMO gaps.

Isomer	Multimembered ring	Component of HOMO (%)	Component of LUMO (%)	HOMO–LUMO gap (eV)
P5	7-Membered ring	30	29	0.4
P6	7-Membered ring	48	55	0.4
	8-Membered ring	12	27	
P7	7-Membered ring	44	50	0.8
	8-Membered ring	11	8	
P8	7-Membered ring	59	65	0.4
P9	7-Membered ring	54	64	0.6
	8-Membered ring	23	4	
P10	7-Membered ring	51	39	0.5
	8-Membered ring	16	7	
P11	7-Membered ring	58	51	0.3
P12	7-Membered ring	63	44	0.2
P13	7-Membered ring	60	40	0.2
P14	7-Membered ring	54	47	0.3
P15	7-Membered ring	57	43	0.3
P16	7-Membered ring	55	40	0.5
P17	7-Membered ring	52	44	0.2
P18	7-Membered ring	51	34	0.4
P19	7-Membered ring	56	30	0.5
P20	7-Membered ring	43	57	0.1
P21	7-Membered ring	45	29	0.5
P22	7-Membered ring	30	30	0.6
P23	7-Membered ring	26	17	0.5

Table 8 summarizes the contribution of the 7- and 8-membered rings to the HOMO and LUMO for all the isomers except P1–P4 and P24 isomers that have no the two rings, together with the HOMO-LUMO gap. Tables 7 and 8 indicate that both rings contribute to the HOMO and LUMO and the amount of their

contribution tends to be proportional to their numbers included in each isomer. In addition, it is seemed that the isomers with only many 7-membered rings tend to have a smaller gap, while those with not only 7-membered but also 8-membered rings tend to have a larger gap.

To understand how the 7- and 8-membered rings affect the HOMO–LUMO gap of the C_{120} isomers more clearly, we chose P20, P17, and P13 isomers as a representative with a smaller gap. On the other hand, we chose P7, P9, and P10 isomers as that with a larger gap. Figure 20 compares the HOMO and LUMO wavefunctions with the effective charges for P7, P9, P10, P13, P17, and P20 isomers. Here, the effective charges colored by red and blue denote electron-rich (negative) and electron-poor (positive), respectively.

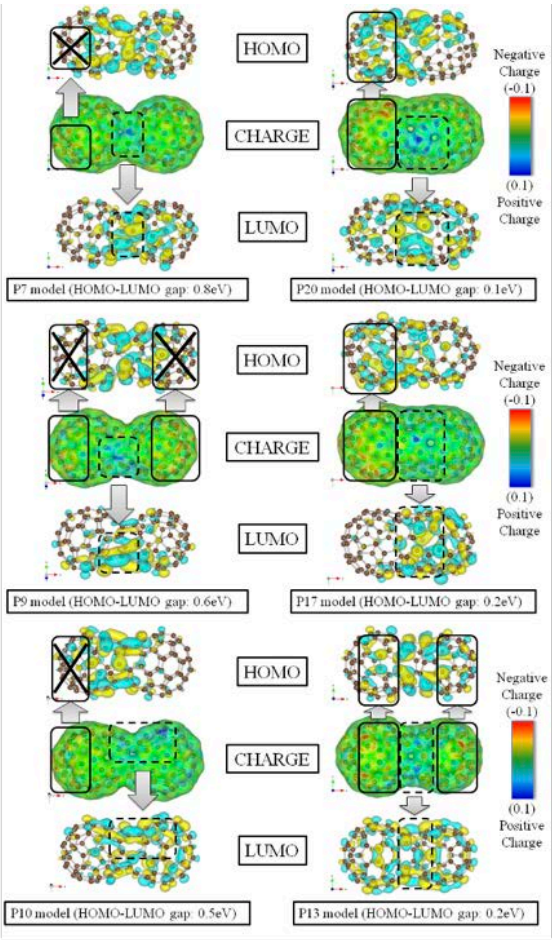


Figure 20. The correlation between the HOMO/LUMO wavefunction and effective charges for P7, P9, P10, P13, P17, and P20 isomers, where the red area of effective charges indicates negative charges (Maximum: -0.1) and the blue area indicates positive charges (Minimum: 0.1).

Comparison between the wavefunctions and effective charges suggests that the location of the HOMO and LUMO wavefunctions corresponds well to that of negative and positive effective charges for P13, P17, and P20 isomers, respectively. On the other hand, the location of the LUMO wavefunction

corresponds to that of the positive effective charges, whereas the location of the HOMO wavefunction not to that of negative effective charges for P7, P9, and P10 isomers.

Figure 21 shows the energy level of the HOMO and LUMO for P7, P9, P10, P13, P17, and P20 isomers. It is found that the difference in the HOMO-LUMO gap among them is mainly due to the difference in individual HOMO levels. Accordingly, it is important to reveal the role of both membered rings in the HOMO energy level of each isomer.

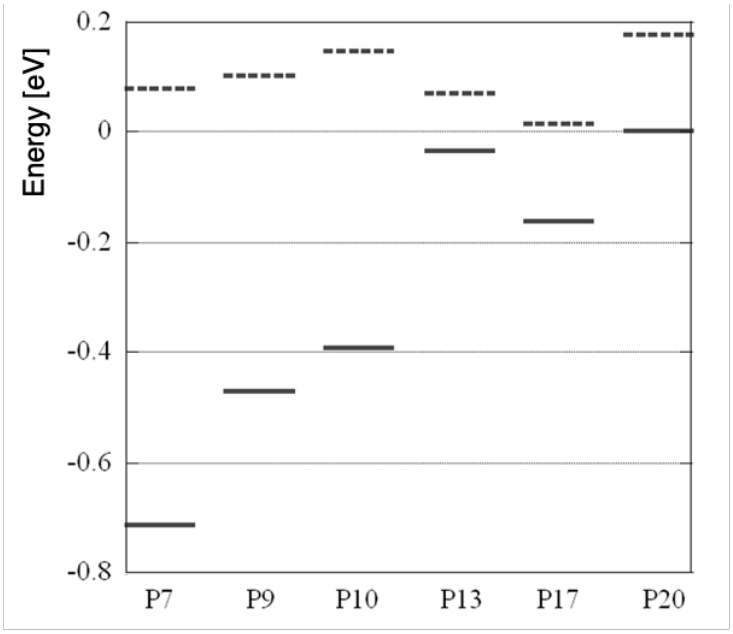


Figure 21. The energy level of the HOMO (solid line) and LUMO (dashed line) for P7, P9, P10, P13, P17, and P20 isomers.

Figure 22 shows the location of each membered ring in the effective charge map for P7, P9, P10, P13, P17, and P20 isomers, where the solid and dashed circles mark the 7- and 8-membered rings, respectively. As shown in Fig. 22, both membered rings are not isolated but next to each other for all the isomers. This figure shows that the polarization degree of P13, P17, and P20 isomers with three 7-membered rings in the waist region was greater than that of P7, P9, and P10 isomers with not only 7-membered rings but an 8-membered ring. This tendency can be seen for other isomers, because Table 9 shows that almost the 7-membered rings have positive effective charges, while the 8-membered ring has negative ones for all the isomers. The difference in their polarization degrees may be due to the fact that the 8-membered ring with negative charges, which is located next to the 7-membered rings, reduces their positive charges.

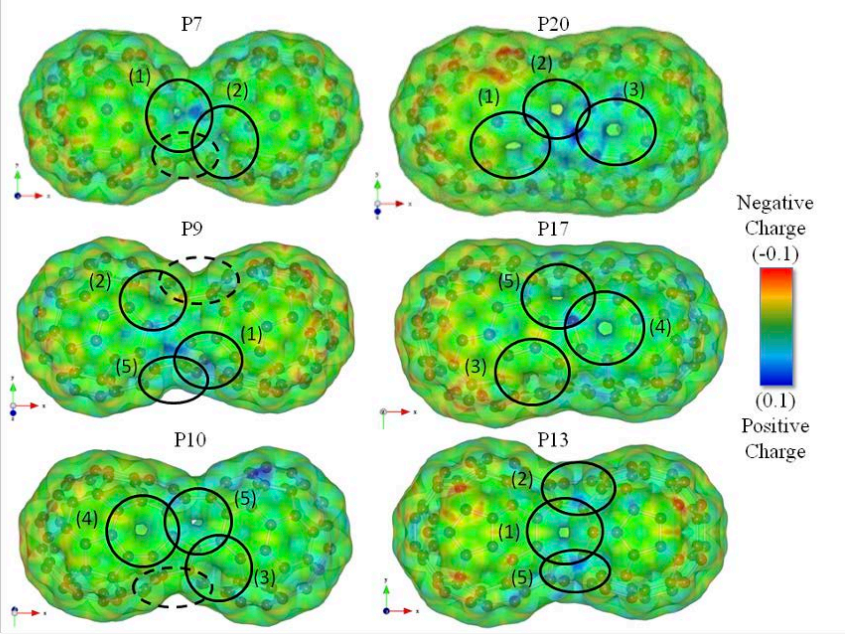


Figure 22. The effective charges and location of the 7-membered (solid circle) and 8-membered (dash circle) rings for P7, P9, P10, P13, P17, and P20 isomers, where the red area of effective charges has negative charges (Maximum: -0.1) and the blue one has positive charges (Minimum: 0.1).

Table 9. The effective charges on the 7- and 8-membered rings for 19 stable isomers (P5-P23). The P1-P4 and P24 isomers have no 7- and 8-membered rings. Only P6, P7, P9, and P10 isomers have not only 7-membered rings but also one 8-membered ring.

	7-Membered ring (1)	7-Membered ring (2)	7-Membered ring (3)	7-Membered ring (4)	7-Membered ring (5)	7-Membered ring (6)	7-Membered ring (7)	8-Membered ring
P5 Isomer	+0.00	+0.12	-	-	-	-	-	-
P6 Isomer	+0.04	+0.05	+0.00	+0.05	-	-	-	-0.02
P7 Isomer	+0.07	+0.06	+0.04	+0.00	-	-	-	-0.06
P8 Isomer	+0.05	+0.03	+0.05	+0.04	+0.08	-	-	-
P9 Isomer	+0.09	+0.01	0.00	+0.06	+0.05	-	-	-0.03
P10 Isomer	+0.03	+0.03	+0.04	+0.05	+0.06	+0.06	-	-0.02
P11 Isomer	+0.03	+0.02	0.00	+0.05	+0.08	+0.01	-	-
P12 Isomer	+0.05	-0.03	-0.02	+0.04	+0.03	0.00	+0.11	-
P13 Isomer	+0.08	+0.06	+0.06	+0.03	+0.08	-	-	-
P14 Isomer	+0.06	+0.06	+0.07	+0.04	+0.07	-	-	-
P15 Isomer	+0.02	+0.04	+0.02	+0.04	+0.08	+0.07	-	-
P16 Isomer	+0.03	+0.07	+0.03	+0.06	+0.08	-	-	-
P17 Isomer	+0.08	+0.02	+0.02	+0.08	+0.03	-	-	-
P18 Isomer	+0.02	+0.02	+0.05	-	-	-	-	-
P19 Isomer	+0.04	+0.07	+0.08	-	-	-	-	-
P20 Isomer	+0.05	+0.09	+0.12	+0.04	-	-	-	-
P21 Isomer	+0.05	+0.05	+0.03	+0.07	-	-	-	-
P22 Isomer	+0.02	+0.09	+0.04	+0.02	-	-	-	-
P23 Isomer	+0.03	+0.03	-	-	-	-	-	-

The P1–P4 and P24 isomers have no 7- and 8-membered rings. Only P6, P7, P9, and P10 isomers have not only 7-membered rings but also one 8-membered ring.

From the results of Table 9 and Fig. 22, the polarization degree for the isomers with a smaller HOMO-LUMO gap is greater than that for those with a larger gap. In addition, Figure 20 shows that the

location of the HOMO wavefunction is overlapped well with that of the negative effective charges. Presumably, such the large negative charges enlarge the electron-electron interactions in the HOMO for P13, P17, and P20 isomers, which make the HOMO energy level higher than that for P7, P9, and P10 isomers, as shown in Fig. 21. Consequently, the polarization induced by the adjacent 7-membered rings enhances the electron-electron repulsive interactions, which makes the HOMO level higher. This reduces the HOMO-LUMO gap of the C_{120} isomer.

7. Optical transitions of Fe, Co, and Ni ferrocyanides (MFCs)

M(III) ferrocyanides (MFCs), which have a jungle gym structure shown in Fig. 23, are one of metal-organic-framework (MOF) materials with many fascinating features [111]. FeFC (Prussian blue: PB) and the other MFCs have been extensively studied from both fundamental and industrial aspects [112, 113]. Indeed, it is still fresh in our memories that S. Kitagawa won the Nobel prize in chemistry in 2025. Since MFCs can be easily synthesized by mixing M complexes with $[Fe(II)(CN)_6]^{4-}$ aqueous solution and have a variety of electronic and spin states, they have been applied to color inks [114], Cesium (Cs) adsorbents [115, 116], optical recording devices[117], etc.

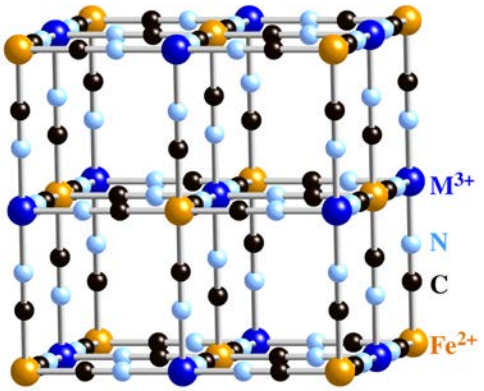


Figure 23. Schematic illustration of the crystal structure of M(III) ferrocyanides (M=Fe, Co, Ni), in which divalent iron (Fe^{2+}) and trivalent metal (M^{3+} = Fe^{3+}, Co^{3+}, Ni^{3+}) are bridged *via* the CN^- anion.

Recently, we have focused on the MFCs as an adsorbent for Platinum-group metals (PGMs) such as Ruthenium (Ru), Rhodium (Rh) and Palladium (Pd) contained in a high-level radioactive nuclear liquid waste (HLLW), because these elements have significantly negative effects in the vitrification processes of HLLW [118]. Namely, PGMs have the property of not dissolving into glass, which degrades the quality of vitrified wastes. One way to solve these issues is to remove PGMs from HLLW prior to putting them into

the glass melter by using MFCs, because PB have been reported to be a good adsorbent for Cs^+ ions [115, 116]. However, to the best of our knowledge, there have been no reports on the adsorption mechanisms of PMGs to MFCs so far. Judging from the structure of MFCs shown in Fig. 23, three possible mechanisms can be speculated: (i) surface adsorption (Langmuir type) on the CN anion group, (ii) insertion to the space of the jungle gym, and (iii) substitution to M(III) or Fe(II) in the framework of MFCs.

To clarify the adsorption mechanisms of PGMs to MFCs, it is important to understand the electronic properties of MFCs prior to their adsorptions. The accurate expression of the electronic structures for MFCs is, however, quite difficult. The overall feature of the absorption spectra for MFCs is significantly influenced both by the strong correlations among localized 3d electrons and by correlations between the electrons for adjacent metals *via* a cyano-group. To solve the issues, first-principles method based on the many-electron calculation is absolutely imperative for explaining the electronic structure of MFCs. Such these correlated systems have been also studied by DFT calculations with the generalized gradient approximation (GGA) + *U* correction method or the hybrid functional method [119–122]. However, when used within the one-electron approximation, these methods are still hard to discuss the multiplet structures and optical properties of the strongly correlated systems. Ogasawara, Adachi, and some other groups have investigated the optical properties of the strongly correlated systems using a first-principles many-electron method [123–128], and successfully discussed their multiplet-energy levels and optical properties.

Thus, we have investigated the multiplet energy levels and absorption spectra of typical MFCs (M = Fe, Co, Ni) using ultraviolet visible (UV-vis) absorption spectroscopy and first-principles relativistic many-electron calculations [29]. The UV-vis absorption spectra of MFCs were investigated using the relativistic configuration interaction (CI) method [123, 127]. In this first-principles CI calculation, the multiplet energy levels and absorption spectra were calculated using $Fe^{2+}M^{3+}(CN^-)_{11}{}^{6-}$ (M^{3+} = Fe^{3+}, Co^{3+}, Ni^{3+}) model cluster. The structural parameters of these model clusters were determined from the optimized structures estimated by the CASTEP code [129-131].

In the first-principles CI calculations, four-component relativistic molecular orbital (MO) spinors were obtained using relativistic DFT calculations, in which the four-component Dirac equation was solved numerically. These four-component relativistic MO spinors were expressed as linear combinations of atomic orbital (LCAO) spinors [36]. In the present calculations, we used the relativistic formalism of the Vosko-Wilk-Nusair (VWN) exchange-correlation potential, $V_{xc}(\mathbf{r})$, within the local density approximation (LDA), which was proposed by MacDonald and Vosko (RVWN) [132].

After the one-electron relativistic DFT calculations, many-electron calculations were performed using

the relativistic MO spinors. Since the CI calculations for all N electrons in a cluster required a prodigious quantity of computational time and resources, only MOs mainly composed of Fe^{2+}-3d and M^{3+}-3d orbitals were explicitly considered in the many-electron calculations.

The many-electron Dirac-Coulomb-Breit Hamiltonian, H_{DCB}, can be expressed as,

$$H_{\mathrm{DCB}} = \sum_{i}^{n} h_{\mathrm{D}}(\mathbf{r}_i) + \sum_{i}^{n}\sum_{j>i}^{n}\left[\frac{1}{r_{ij}} - \frac{1}{2r_{ij}}\left\{\boldsymbol{\alpha}_i \cdot \boldsymbol{\alpha}_j + \frac{(\boldsymbol{\alpha}_i \cdot \mathbf{r}_{ij})(\boldsymbol{\alpha}_j \cdot \mathbf{r}_{ij})}{r_{ij}^2}\right\}\right] \qquad (8),$$

where n is the number of electrons in the active space of the CI calculations, and $\mathbf{r}_i$ is the position of the i-th electron. The first and second terms of H_{DCB} represent the one-electron and two-electron operators, respectively. The one-electron Dirac operator h_{D} can be expressed as,

$$h_{\mathrm{D}}(\mathbf{r}_i) = c\tilde{\boldsymbol{\alpha}}\mathbf{p}_i + \tilde{\beta}c^2 - \sum_{v}\frac{Z_v}{|\mathbf{r}_i - \mathbf{R}_v|} + V_0(\mathbf{r}_i) \qquad (9),$$

where c is the velocity of light, $\mathbf{p}_i$ is the momentum operator, $\tilde{\boldsymbol{\alpha}}$ and $\tilde{\beta}$ are the Dirac matrices, Z_v and $\mathbf{R}_v$ are the charge and position of the v-th nucleus, respectively. $V_0(\mathbf{r}_i)$ in Eq. (9) denotes the Coulomb and exchange-correlation potentials on these explicitly treated electrons from the other (core and valence) electrons. This potential $V_0(\mathbf{r}_i)$ is expressed as,

$$V_0(\mathbf{r}) = \int \frac{\rho_0(\mathbf{r}')}{|\mathbf{r} - \mathbf{r}'|}\mathrm{d}\mathbf{r}' + \left[\frac{\rho(\mathbf{r})\varepsilon_{\mathrm{XC}}\{\rho(\mathbf{r})\} - \rho_0(\mathbf{r})\varepsilon_{\mathrm{XC}}\{\rho_0(\mathbf{r})\}}{\rho_{\mathrm{imp}}(\mathbf{r})} - \varepsilon_{\mathrm{XC}}\{\rho_{imp}(\mathbf{r})\}\right] \qquad (10),$$

where ρ_{imp} is the charge density of the selected n electrons, ρ_0 is the charge density of the other $N - n$ electrons, ρ is the charge density of all N electrons ($\rho = \rho_0 + \rho_{\mathrm{imp}}$), and $\varepsilon_{\mathrm{XC}}$ is the RVWN exchange-correlation energy.

The two-electron operator, the second term of eq. (8), represents electron-electron repulsion between electrons occupying the Fe^{2+} and M^{3+}-3d states explicitly. The electron-electron repulsion term following $1/r_{ij}$ is known as the frequency-independent Breit operator [133, 134]. The Breit operator contains the magnetic interactions originating from orbital and spin motions. The finite transmission speed of the signal between particles (electrons), which is generally regarded as the retardation effect, is also taken into account. By diagonalizing the many-electron Hamiltonians shown in eq. (8), one can obtain the many-electron eigenvalues and corresponding eigenvectors. Many-electron wave functions are generally expressed as a linear combination of Slater determinants,

$$\Psi_i = \sum_{p=1}^{M} C_{ip}\Phi_p \qquad (11),$$

where Ψ_i is the i-th many-electron wave function, Φ_p is the p-th Slater determinant, C_{ip} is a coefficient, and M is the number of Slater determinants. As the active space for the CI calculations, all the electronic

configurations of the 3d-3d intra-transitions for both Fe^{2+} and M^{3+} ions were explicitly treated. On the other hand, the electronic configurations for the CT transitions between Fe^{2+} ion and M^{3+} ions were considered up to two-electron excitations.

The oscillator strength of the electric dipole transition both for the 3d–3d intra-transitions of Fe^{2+} and M^{3+} ions and for the Fe^{2+}–M^{3+} CT transitions averaged over all directions is given by

$$I_{if} = \frac{2}{3}(E_f - E_i)\left|\left\langle \Psi_f \left| \sum_{k=1}^{n} \mathbf{r}_k \cdot \mathbf{e} \right| \Psi_i \right\rangle\right|^2 \qquad (12).$$

Here, Ψ_i and Ψ_f are the many-electron wave functions for the initial and final states, respectively, and E_i and E_f are their corresponding energies [135]. Theoretical spectra were obtained by convolution of the oscillator strength with a Gaussian function with a FWHM of 0.30 eV.

Table 10 summarizes the lattice constants and bond lengths for the three MFCs estimated by DFT calculations with the low-spin (LS) state for Fe^{2+}, Co^{3+} and Ni^{3+}, and the high-spin (HS) state for Fe^{3+}, respectively. In addition, ferromagnetic order was considered for HS Fe^{3+} and LS Ni^{3+} ions.

Table 10. Theoretical lattice constant and each bond length of the three models for MFCs. The unit of length is Å.

FeFC	$Fe[Fe(CN)_6]^-$	$KFe[Fe(CN)_6]$	$CsFe[Fe(CN)_6]$
lattice constant	10.470	10.279	10.306
Fe^{2+}–C	1.905	1.864	1.870
Fe^{3+}–N	2.139	2.086	2.094
C–N	1.191	1.189	1.189
CoFC	$Co[Fe(CN)_6]^-$	$KCo[Fe(CN)_6]$	$CsCo[Fe(CN)_6]$
lattice constant	10.114	9.927	9.962
Fe^{2+}–C	1.917	1.871	1.879
Co^{3+}–N	1.951	1.907	1.909
C–N	1.188	1.185	1.187
NiFC	$Ni[Fe(CN)_6]^-$	$KNi[Fe(CN)_6]$	$CsNi[Fe(CN)_6]$
lattice constant	10.552	10.316	10.352
Fe^{2+}–C	1.930	1.890	1.895
Ni^{3+}–N	2.159	2.083	2.095
C–N	1.188	1.185	1.185

To confirm this, we examined three different types of the magnetic order [120]: ferromagnetic (FM), antiferromagnetic type-I (AF_1), and type-II (AF_2). In the present DFT calculations based on the GGA+*U* method, the difference in total energy among them was too small (less than 0.001 eV) to discuss the magnetic stability of MFCs. The magnetism of FeFC was, however, experimentally reported to exhibit ferromagnetic order at a low temperature [136]. Thus, we considered the ferromagnetic order for HS Fe^{3+}

to calculate the structural parameters and density-of-states (DOS). In addition, since the difference in the lattice constant among the three MFCs was negligibly small to have no effects on the many-electron calculations. As shown in Table 10, the lattice constant of $Fe[Fe(CN)_6]^-$ and $Ni[Fe(CN)_6]^-$ was overestimated by ca. 3 and 4 %, respectively, when compared to their experimental values. This is due to the delocalization of excess electrons. On the other hand, the lattice constant was in reasonably agreement with the experimental one for $KM[Fe(CN)_6]$ and $CsM[Fe(CN)_6]$ (M=Fe, Ni). In the case of CoFC, the lattice parameters for all the models reasonably reproduced the experimental ones. Since the bond length of Fe^{2+}–C was close to each other for all the MFCs as well as that of C–N, the difference in the lattice constant among MFCs used here is mainly caused by a change in M^{3+}–N bond-length.

Figure 24 shows the DOS of FeFC calculated by using the three models: (a) $Fe[Fe(CN)_6]^-$, (b) $KFe[Fe(CN)_6]$, and (c) $CsFe[Fe(CN)_6]$. The Fermi level (E_F) is located at 0 eV along the energy axis. The occupied and unoccupied DOSs are located below and above E_F, respectively. The positive and negative values of DOS indicate the up and down spin states, respectively. The partial DOS indicated by gray, blue, and red denote s, p, and d-orbitals, respectively.

As shown in Fig. 24, the occupied DOS near E_F was dominated by the t_{2g} orbitals of Fe^{2+}, whereas the lowest unoccupied DOS located at around 1.4 eV above E_F by the unoccupied t_{2g} down-spin orbitals of Fe^{3+} for the three models. Thus, the electron excitation between the two occupied and unoccupied DOSs implies the charge-transfer (CT) transitions from the Fe^{2+} occupied states to the Fe^{3+} unoccupied states. Correspondingly, photo-absorption band appears in the visible region. In addition, comparison among the results of Figs. 24 (a)–(c) found that insertion of K^+ or Cs^+ ion to the framework cavities of $Fe[Fe(CN)_6]^-$ has no effects on its valence electronic structure.

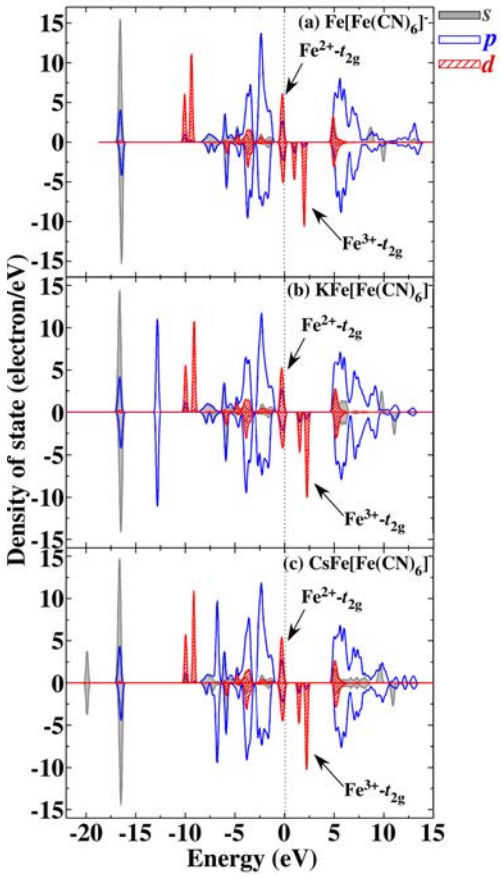


Figure 24. The DOS of FeFC calculated by using the three models: (a) $Fe[Fe(CN)_6]^-$, (b) $KFe[Fe(CN)_6]$, and (c) $CsFe[Fe(CN)_6]$. The E_F is located at 0 eV along the energy axis. The occupied and unoccupied DOSs are located below and above the E_F, respectively. The positive and negative values of DOS indicate the up and down spin states, respectively. The partial DOS curves shown in gray, blue, and red denote s, p, and d-orbital, respectively.

Figure 25 shows the experimental (top) and theoretical (bottom) absorption spectra of FeFC. In the theoretical spectrum, the oscillator strengths of individual peaks are also shown. The overall features of the theoretical absorption spectrum reproduced the main features of the experimental spectrum well, although the absolute multiplet energy levels (transition energy) were overestimated by ca. 1.5–2.0 eV systematically. The overestimation of the multiplet energy can be corrected by performing the Slater's transition-state calculations [56], which is shifted by the orbital energy difference between the single-electron orbitals of the Slater transition-state as a reference [56, 137].

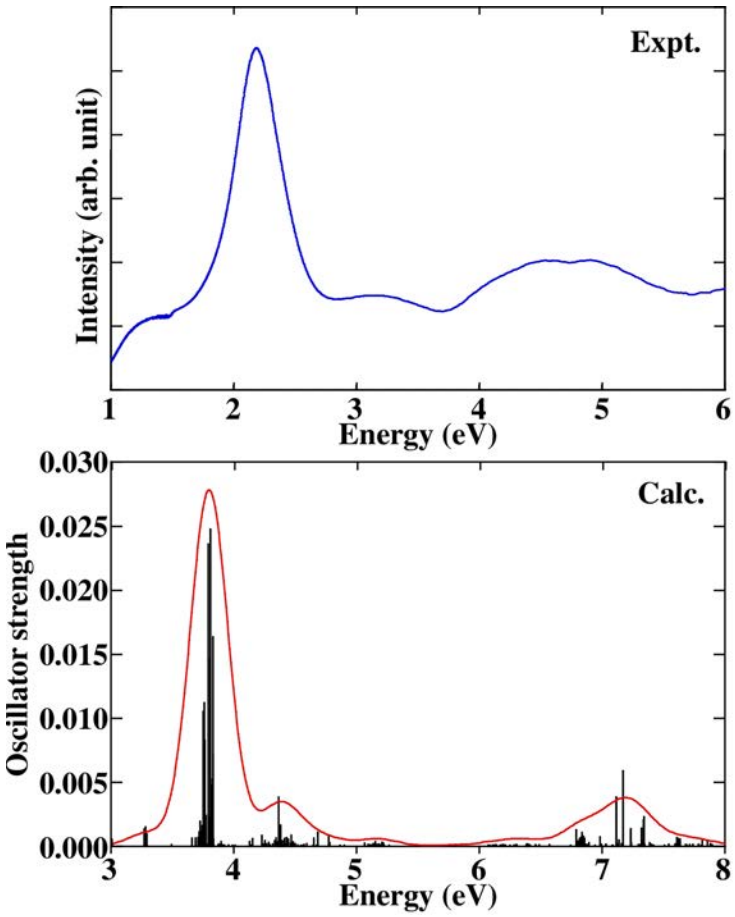


Figure 25. Comparison between the experimental (a) and theoretical (b) absorption spectra of FeFC (Prussian blue) [29].

In order to assign the individual peaks of the theoretical absorption spectrum, configuration analysis of the many-electron wave functions was performed. Figure 26 shows both the oscillator strengths of the transitions from the lowest state and the configuration compositions for each level, together with the corresponding electronic configurations. It is noted that the electronic configurations only relevant to the absorption in the visible region are shown in Fig. 26. The Fe-3d levels split into the t_{2g} and e_g from the lower level according to the irreducible representations of O_h symmetry.

The main component for the ground state (GS) was the $(Fe^{2+}t_{2g})^6(Fe^{2+}e_g)^0(Fe^{3+}t_{2g})^3(Fe^{3+}e_g)^2$ configuration with contribution of the $(Fe^{2+}t_{2g})^5(Fe^{2+}e_g)^0(Fe^{3+}t_{2g})^4(Fe^{3+}e_g)^2$ configuration. This indicates that the Fe^{2+} and Fe^{3+} are LS and HS states for their ground states, respectively. The intense absorption band in the visible region corresponds to the transitions from the GS to the $(Fe^{2+}t_{2g})^6(Fe^{2+}e_g)^0(Fe^{3+}t_{2g})^4(Fe^{3+}e_g)^1$, $(Fe^{2+}t_{2g})^5(Fe^{2+}e_g)^0(Fe^{3+}t_{2g})^4(Fe^{3+}e_g)^2$, and

$(Fe^{2+}t_{2g})^4(Fe^{2+}e_g)^0(Fe^{3+}t_{2g})^5(Fe^{3+}e_g)^2$ configurations, which correspond to the 3d–3d intra-transitions of Fe^{3+} ions, the Fe^{2+}–Fe^{3+} CT transitions, and the two-electron CT excitation states based on a shake-up process, respectively.

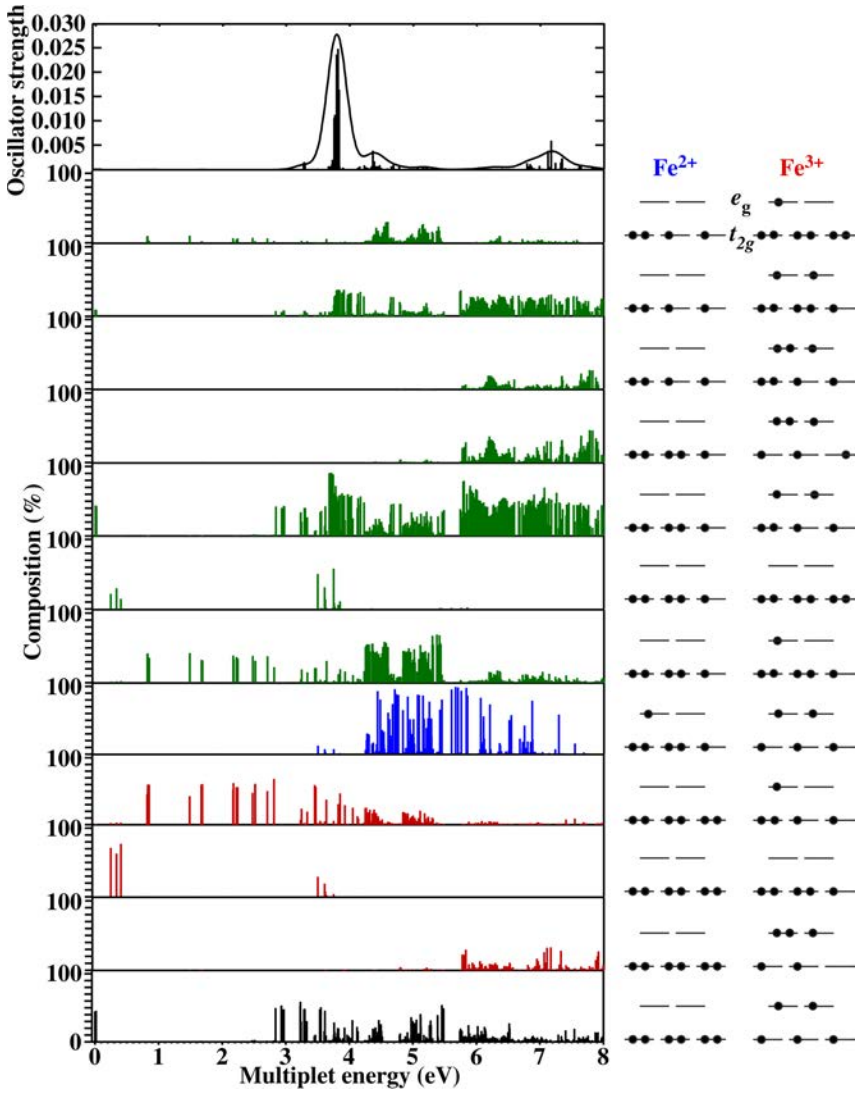


Figure 26. Configuration analysis of the many-electron wave functions for the 3d–3d intra-transitions and Fe^{2+}–Fe^{3+} CT transitions for FeFC. Corresponding electronic configurations are shown in right side.

This indicates that the intense absorption band in the visible region can be attributed not only to the CT transitions from Fe^{2+} to Fe^{3+} ions and but also to the 3d-3d intra-transitions of Fe^{3+} ions. In addition, the energy difference of the spin-crossover for Fe^{3+} ions was estimated to be ca. 0.24–0.40 eV, corresponding to the transitions from the GS $(Fe^{2+}t_{2g})^6(Fe^{2+}e_g)^0(Fe^{3+}t_{2g})^3(Fe^{3+}e_g)^2$ configuration to the $(Fe^{2+}t_{2g})^6(Fe^{2+}e_g)^0$ $(Fe^{3+}t_{2g})^5(Fe^{3+}e_g)^0$ configuration.

In a similar manner, for the CoFC, the absorption peaks in visible region can be attributed to the 3d–3d intra-transitions of Fe^{2+}. For NiFC, in sharp contrast to the other two MFCs, the peaks at low-energy and high-energy region originated from the Ni^{3+} 3d–3d intra-transitions for low-energy and the Fe^{2+} 3d–3d intra-transitions and CT transitions between Fe^{2+} and Ni^{3+} for high energy, respectively. Details of the MFCs (M = Co, Ni) have been discussed elsewhere [29].

In addition, we also succeeded in analyzing the UV-vis spectra of Palladium nitrate complex in nitrate solution using the DV-ME method [30].

8. Uptake characteristics of Prussian Blue for Platinum-group metals

PGMs such as Ru, Rh, and Pd are generated to be 2.1, 0.4, and 1.2 kg, respectively, after burnup of 1 t nuclear fuels (30 GWd/t) in a light-water reactor [138]. After separating uranium (U) and plutonium (Pu) from the spent fuels by using the PUREX (**P**lutonium **U**ranium **R**edox **EX**traction) method in order to reuse them as new fuels, the high-level radioactive liquid wastes (HLLW) are vitrified and geologically disposed [139–141]. As described in the previous section, PGMs included in HLLW have a property of not dissolving into glass in the vitrification processes. This issue degrades the quality and stability of the vitrified objects due to heterogeneity. Thus, it is useful to recover PGMs from HLLW both to improve nuclear-waste management and to recover critical metals.

We have recently investigated the uptake mechanism of PGMs by Prussian blue (PB) nanoparticles (PBNPs) in a nitric acid solution, and revealed from experimental and theoretical results that the PGMs ion is incorporated into PBNPs by substitution with Fe^{2+}/Fe^{3+} ion of the PB framework ($Pd^{2+}\rightarrow Fe^{2+}$, $Rh^{3+}/Ru^{4+}\rightarrow Fe^{3+}$) with maintaining the crystal structure before and after PGMs sorption [33, 142].

Figure 27 shows (a) the experimental spectra with respect to the absorption energy before (black) and after (red) 24 h sorption test [the intensity (absorbance) of the two spectra was normalized at 6 eV], and (b–d) theoretical spectra of the PB model before and after substitution with Fe^{2+} or Fe^{3+} for PGMs ions.

Theoretical absorption spectra of the pristine and PGMs-sorbed PBNPs were obtained using the relativistic configuration interaction (CI) method [124, 127], because the present method has been already confirmed to reproduce the experimental absorption spectra of Fe, Co, and Ni ferrocyanides quantitatively, using $Fe(II)M(III)(CN^{-})_{11}^{6-}$ (M = Fe, Co, Ni) cluster model [29]. The multiplet energy levels and absorption spectra were calculated using $Fe^{2+}Fe^{3+}(CN^{-})_{11}^{6-}$, $MFe^{3+}(CN^{-})_{11}^{6-}$, and $Fe^{2+}M(CN^{-})_{11}^{6-}$ cluster models (M = Ru^{4+}, Rh^{3+}, Pd^{2+}) [see Fig. 27], respectively, for the pristine and PGMs-sorbed PBNPs. Here, when the PBNPs are applied to the disposal of HLLW in a strong nitric acid solution (2–8 M), the present calculations were performed using an oxidation ionic valence of 4+, 3+, and 2+ for Ru, Rh, and

Pd, respectively. The choice of the valence values for these ions is reasonable, because the valence of each ion in the nitric acid solution has been already clarified experimentally [30, 32, 143, 144]. The structural parameters of these cluster models were determined from the optimized structures obtained using DFT calculations. Details of the CI calculation method were described elsewhere [124, 127]. As the active space for the CI calculations, all the electronic configurations of the d–d transitions for Fe and PGMs ions were explicitly treated. On the other hand, the electronic configurations for the charge transfer (CT) transitions from Fe^{2+}/M to M were considered up to two electron excitations. The oscillator strength of the electric dipole transitions averaged over all directions was obtained using the general equation expressing the electric dipole transition. Theoretical absorption spectra were obtained by convolution of the oscillator strength replaced with a 0.30 eV FWHM of Gaussian function.

As shown in Fig. 27, for the pristine PBNPs, the three absorption bands around 1.6 eV (weak), 2.1 eV (intense), 3.1 eV (weak), and 5.0 eV (middle) originate from the CT transitions from Fe^{2+} to Fe^{3+}, which correspond to peaks A, B, C, and D, respectively [29]. For Pd ion (right hand), the theoretical spectra of the Pd ion substituted with Fe^{2+} (c) well explain the experimental spectral change (red shift) when compared to the spectra of the Pd ion substituted with Fe^{3+} (d). This is consistent with the previous results obtained using CASTEP [131]. For Rh ion (the middle-right panel), comparison in theoretical spectra between before (b) and after (c, d) Rh substitution indicates that spectra (d) obtained for Rh substituted with Fe^{3+} reasonably explain the experimental spectral change after Rh sorption test. Thus, it is reasonable to be concluded that Rh ion is mainly substituted with Fe^{3+} ion. For Ru ion (the middle-left panel), comparison in theoretical spectra between before (b) and after (c, d) Ru substitution indicates that spectra (d) obtained for Ru substituted with Fe^{3+} obviously explain the experimental spectral change after Ru sorption test, because no red-shift in spectra after Ru sorption test was observed experimentally. In summary, it is reasonably concluded from the results of Fig. 27 that Ru^{4+} and Rh^{3+} ions are substituted with Fe^{3+} ion, whereas Pd^{2+} ion is substituted with Fe^{2+} ion [142].

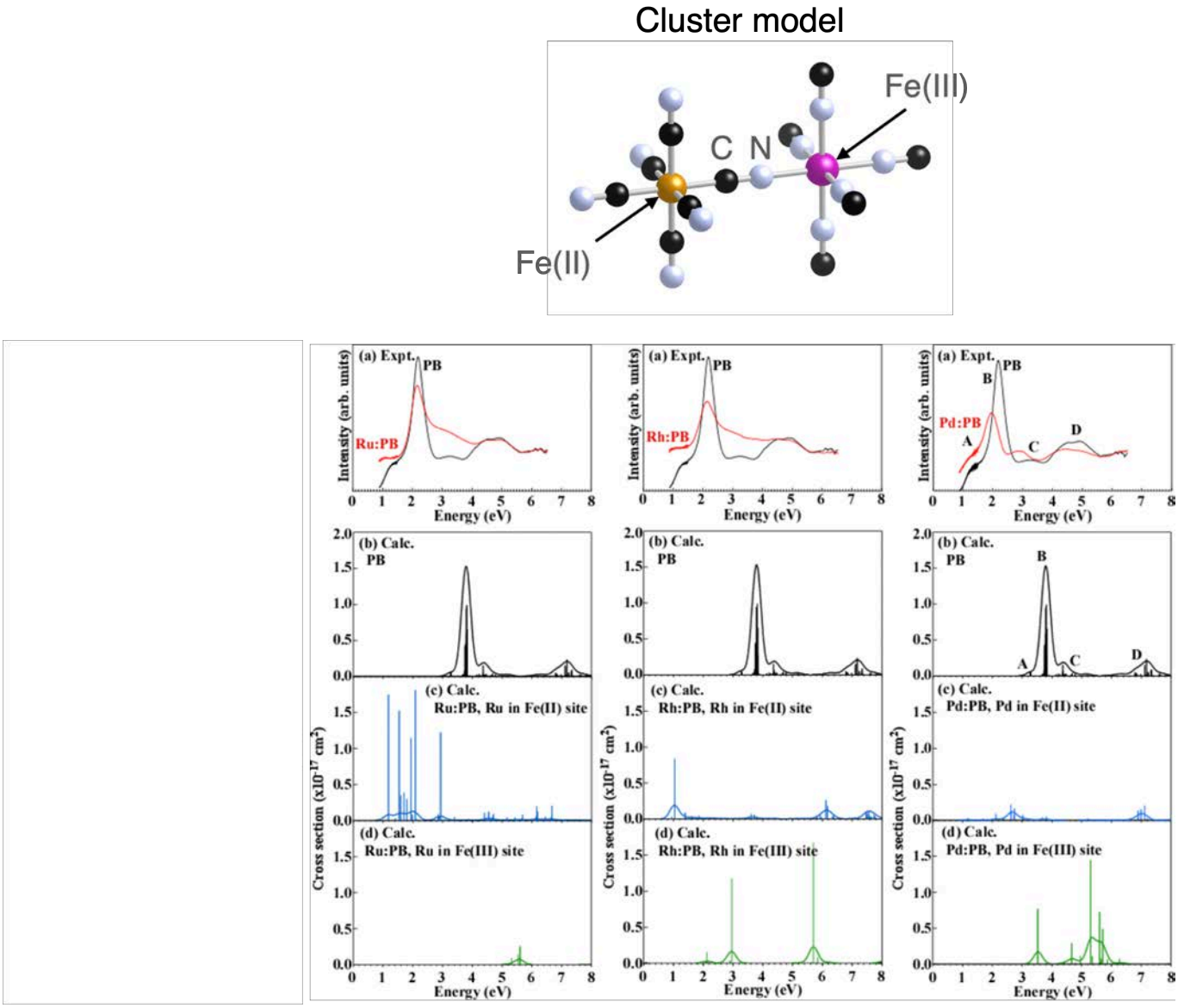


Figure 27. Theoretical spectra of the pristine (b) and PGMs-sorbed PB using the cluster models for Fe^{2+} (c) and Fe^{3+} (d) substitution, along with the experimental UV-vis-NIR spectra of PB before (black) and after (red) PGMs sorption (a).

9. Summary and Outlook

9.1. Summary

This review has demonstrated the versatility of the DV-Xα MO method and its extensions, the DV-DS and DV-ME methods, in elucidating the relationships among electronic structure, chemical bonding, spectroscopic properties, and materials functionality. The applications discussed here extend from uranium compounds and actinide alloys to nanocarbon materials, transition-metal ferrocyanides, and

metal-ion separation systems. Collectively, these studies illustrate the value of a computational approach that connects AO interactions with experimentally observable properties.

A principal strength of DV-Xα and DV-DS methods is their ability to provide chemically interpretable descriptions of molecular orbitals and chemical bonding in finite clusters. Atomic-orbital populations and bond overlap populations enable individual bonding and antibonding interactions to be examined directly. This information has been particularly useful in clarifying the influence of relativistic effects on uranium compounds. For example, the analysis of UF_6 and UF_5 demonstrates how relativistic orbital contraction and expansion alter the contributions of uranium 5f, 6s, 6p, and 6d orbitals to U–F bonding. Such orbital-resolved interpretations provide a complementary perspective to total energies, band structures, and density-of-states calculations.

The relativistic DV-DS formalism is especially important for compounds containing heavy elements, for which spin–orbit coupling and other relativistic effects can substantially influence electronic structures and chemical bonding. The applications to uranium complexes, uranium carbide, metallic uranium, and uranium–transition-metal alloys further illustrate how cluster calculations can connect local orbital interactions with chemical stability, spectroscopic assignments, and alloying behavior.

The scope of these approaches has also expanded beyond conventional one-electron molecular-orbital analysis. Although DV-Xα and DV-DS are useful for interpreting orbital energies and bonding, a one-electron approximation alone cannot adequately describe all multiplet structures and optical transitions for strongly correlated systems. The DV-ME approach addresses this limitation by explicitly treating selected many-electron configurations using relativistic molecular spinors. Its application to transition-metal ferrocyanides therefore provides a route to interpreting multiplet energy levels and optical absorption in materials containing localized 3d electrons.

More recently, the combination of spectroscopy and electronic-structure calculations has provided a molecular-level framework for investigating platinum-group-metal ions in nitric acid solutions and their interactions with Prussian-blue-based materials. These studies demonstrate the potential of the DV approach to contribute to the understanding of selective metal-ion uptake and resource recovery. In this context, the method serves not merely as a tool for assigning spectra but also as a means of formulating chemically informed hypotheses concerning material selectivity.

9.2. Comparison with General-Purpose Electronic-Structure Programs

Table 11 compares the characteristics of DV-Xα/DV-DS/DV-ME approaches with those of widely used electronic-structure software packages such as Gaussian [145], CASTEP [131], and VASP [146, 147].

Table 11. Comparison of DV-Xα/DV-DS/DV-ME approaches with widely used electronic-structure software packages.

Feature	DV-Xα/DV-DS/DV-ME	Gaussian [145]	CASTEP [131]	VASP [146, 147]
Computational framework	Discrete-variational molecular-orbital and many-electron methods	Molecular quantum chemistry	Periodic plane-wave DFT	Periodic plane-wave DFT
Model systems	Molecules, coordination complexes, embedded clusters, finite fragments of solids	Molecules, ions, and finite clusters	Crystals, surfaces, and periodic materials	Crystals, surfaces, interfaces, and periodic materials
Basis set	Numerically generated atomic orbitals and discrete variational sampling	Primarily atom-centered basis sets; additional basis representations are available	Plane waves with pseudopotentials or related approaches	Plane waves with projector augmented-wave (PAW) datasets
Relativistic effects	DV-DS explicitly incorporates the Dirac equation and spin–orbit effects; DV-ME can use relativistic molecular spinors	Relativistic treatments are available, depending on the method and basis or effective-core-potential approach	Relativistic effects can be included through suitable pseudopotentials and spin–orbit calculations	Relativistic effects can be included through suitable PAW datasets and spin–orbit calculations
Chemical-bonding interpretation	Direct analysis of atomic-orbital contributions, orbital populations, and bond overlap populations	Orbital and population analyses are available; interpretation depends on the selected method	Projected densities of states, charge densities, and related bonding analyses	Projected densities of states, charge densities, and related bonding analyses
Strongly correlated electrons	DV-Xα/DV-DS provide one-electron descriptions; DV-ME explicitly treats selected many-electron configurations and multiplet states	Electron correlation can be treated using methods such as configuration interaction and coupled-cluster theory, subject to system size	DFT, DFT+U, hybrid functionals, and other supported approaches; explicit multiplet treatment generally requires additional methods	DFT, DFT+U, hybrid functionals, and other supported approaches; explicit multiplet treatment generally requires additional methods
Spectroscopic interpretation	Particularly suited to orbital-resolved interpretation of XPS and, with DV-ME, multiplet energies and optical transitions	Extensive molecular spectroscopy and excited-state capabilities	Periodic electronic structures, optical response, and related solid-state properties	Periodic electronic structures, optical response, and related solid-state properties
Large periodic systems	Cluster-based rather than intrinsically periodic; cluster size and boundary effects must be considered	Periodic calculations are not its principal conventional workflow	Particularly suitable for periodic materials and crystalline properties	Particularly suitable for periodic materials and crystalline properties
Distinctive research role	Chemically transparent orbital-level analysis, relativistic cluster calculations, and selected many-electron spectroscopy	Broad molecular chemistry and diverse correlated wavefunction methods	Periodic materials modeling and structural/property prediction	Periodic materials modeling, electronic-structure calculations, and atomistic simulations

Widely used packages such as Gaussian, CASTEP, and VASP offer extensive capabilities for molecular quantum chemistry and periodic materials simulations. Gaussian supports a broad range of molecular electronic-structure methods, including DFT and correlated wavefunction approaches. CASTEP and VASP are particularly well suited to periodic systems, including crystals, surfaces, and interfaces, and provide powerful tools for investigating structural stability, electronic bands, and material properties.

The objective of the DV-Xα/DV-DS/DV-ME framework is not to replace these programs. Rather, it is to address complementary scientific questions. In particular, DV-Xα and DV-DS offer a direct route to examining how individual AOs contribute to bonding in finite clusters, whereas DV-DS incorporates a relativistic Dirac–Slater description. DV-ME extends this framework to selected many-electron states, enabling explicit analyses of multiplet structures and optical transitions that are not generally obtained

from conventional one-electron calculations alone. These capabilities make the DV approaches particularly attractive when the interpretation of local electronic interactions is as important as the prediction of macroscopic properties.

Nevertheless, the cluster-based character of the DV methods imposes limitations. Periodic boundary conditions, extended band structures, and large-scale structural relaxation are more naturally handled by periodic electronic-structure packages. Furthermore, the accuracy of any calculation depends on the adopted Hamiltonian, exchange-correlation treatment, cluster construction, and treatment of electron correlation. The DV-Xα approximation should therefore not be assumed to provide universally superior quantitative accuracy. Instead, its principal value lies in the chemically transparent interpretation of electronic structures and in its ability to complement other computational methods.

9.3. Outlook

Future developments should emphasize the integration of DV-Xα/DV-DS/DV-ME calculations with periodic density-functional theory, spectroscopy, and materials experiments. Periodic calculations using CASTEP or VASP can provide optimized structures and information on extended electronic states, whereas subsequent DV calculations on appropriately constructed clusters can investigate local bonding, orbital contributions, and relativistic effects in greater chemical detail. For strongly correlated transition-metal systems, DV-ME calculations can then be employed to examine multiplet energies and optical transitions using selected active spaces. Such a multiscale strategy would exploit the complementary strengths of periodic and cluster-based approaches.

A second promising direction is the application of these methods to functional materials for environmental remediation and resource recovery. In Prussian-blue-based materials, for example, the electronic interactions among transition-metal centers, cyanide ligands, and adsorbed metal ions may influence ion uptake and selectivity. Combining spectroscopic measurements, structural characterization, and orbital-resolved calculations could help distinguish possible adsorption mechanisms and identify the electronic factors governing selective uptake. Similar approaches may be extended to coordination materials, catalysts, and other systems containing localized d- or f-electrons.

Finally, the systematic development of reproducible computational protocols, improved treatments of electron correlation, and direct comparison with quantitative experimental data will be essential for expanding the predictive utility of the DV methods. Their continued relevance will depend not on competing with every capability of general-purpose software, but on addressing questions for which an explicit understanding of AO interactions, relativistic effects, and many-electron states is indispensable.

In conclusion, DV-Xα, DV-DS, and DV-ME constitute a complementary family of electronic-structure

methods that bridges MO interpretation, relativistic quantum chemistry, correlated-electron spectroscopy, and functional-materials research. Their greatest potential lies in combining chemically intuitive analysis with modern computational and experimental techniques to develop a deeper understanding of materials and to guide the design of materials with targeted properties.

Acknowledgments

The author (J.O.) is deeply thankful to all collaborators such as Emeritus Profs. T. Mukoyama and H. Adachi (Kyoto University), the late Dr. H. Nakamatsu (Kyoto University), Prof. R. Sekine (Shizuoka University), and the late Dr. K. Takeuchi (The Institute of Physical and Chemical Research) for UF_6/UF_5 molecules, to the late Dr. M. Kurihara and Dr. M. Hirata (Japan Atomic Research Agency) for uranium complexes and compounds, and to Drs. A. Takashima (Idemitsu Co., Ltd.) and T. Nishii (Electric Power Development Co., Ltd.) for nanocarbons and to Dr. S. Watanabe (AGC Inc.) for Prussian blue and platinum-group metals. In addition, the author also thanks Emeritus Prof. H. Wakita (Fukuoka University) for encouraging him to submit the present review to Bull. Soc. DV-Xα at DV-Xα annual meeting in Fukuoka this September.

Finally, I received the sad news that Emeritus Prof. Mukoyama passed away on Oct. 21, 2026. I would like to express my deepest gratitude for his long-standing and significant contributions to the Society of Discrete Variational Xα and to the promotion of exchange between Japan and Hungary. It was an honor to have him serve as the primary supervisor for my doctoral degree and to have had the opportunity to engage in collaborative research with him. May he rest in peace.

Biography of the author



Jun Onoe received his master's degree in Chemistry from Osaka University in 1987, and joined Panasonic Co. Ltd in the same year. He moved to RIKEN (The Institute of Physical and Chemical Research) in 1990 and received his Ph.D. in Physics from Kyoto University in 1997. Thereafter, he moved to Tokyo Institute of Technology (Institute of Science Tokyo at present) as an associate professor in 2002, and has been a full professor at Nagoya University since 2014. His current research interests include (1) an interdisciplinary between modern geometry and materials science, (2) Energy harvesting such as organic solar cells and thermoelectric devices, and (3) nanospace materials applied to recover critical metals from nuclear and electronic wastes.

References

[1] J.C. Slater, *Phys. Rev.* **81**, 385 (1951).

[2] J.C. Slater, *Adv. Quantum Chem.* **6**, 1 (1972).

[3] H. Adachi, M. Tsukada, and C. Satoko, *J. Phys. Soc. Jpn.* **45**, 875 (1978).

[4] C. Satoko, M. Tsukada, and H. Adachi, *J. Phys. Soc. Jpn.* **45**, 1333 (1978).

[5] H. Adachi et al., *J. Phys. Soc. Jpn.* **47**, 1528 (1979).

[6] H. Adachi and K. Taniguchi, *J. Phys. Soc. Jpn.* **49**, 1944 (1980).

[7] H. Adachi, T. Mukoyama, and J. Kawai eds, "*Hartree-Fock-Slater Method for Materials Science*: *The DV-Xα Method for Design and Characterization of Materials*", Springer, Berlin/Heidelberg (2006).

[8] H. Adachi *et al*. eds, *Adv. Quantum Chem*. **42** (2003) as a special issue.

[9] P. Pyykkö, *Chem. Rev.* **88**, 563 (1988).

[10] A. Das, U. Das, and K. Das, *Coord. Chem. Rev.* **479**, 215000 (2023).

[11] J. Onoe *et al*., *J. Electron Spectrosc. Relat. Phenom.* **60**, 29 (1992).

[12] J. Onoe *et al*., *Chem. Phys. Lett.* **196**, 636 (1992).

[13] J. Onoe *et al*., *J. Chem. Phys.* **99**, 6810 (1993).

[14] J. Onoe *et al*., *Chem. Phys. Lett.* **217**, 61 (1994).

[15] J. Onoe, *Adv. Quantum Chem*. **37**, 311 (2000).

[16] J. Onoe *et al*., *J. Electron Spectrosc. Relat. Phenom.* **70**, 89 (1994).

[17] J. Onoe *et al*., *Inorg. Chem.* **36**, 1934 (1997).

[18] M. Hirata *et al*., *J. Electron Spectrosc. Relat. Phenom.* **83**, 59 (1997).

[19] M. Hirata *et al.*, *J. Alloys Compd.* **271**–**273**, 128 (1998).

[20] M. Hirata *et al.*, *Adv. Quantum Chem.* **37**, 325 (2000).

[21] M. Hirata *et al*., *Adv. Quantum Chem.* **37**, 335 (2000).

[22] M. Kurihara *et al*., *J. Alloys and Compd.* **283**, 128 (1999).

[23] M. Kurihara *et al.*, *J. Nucl. Mater.* **281**, 140 (2000).

[24] M. Kurihara *et al*., *J. Nucl. Mater.* **326**, 75 (2004).

[25] M. Kurihara *et al.*, *Prog. Nucl. Energy* **50**, 549 (2008).

[26] M. Kurihara, J. Onoe, M. Hirata, and C. Suzuki, *J. Alloys and Compd.* **509**, 1152 (2011).

[27] M. Kurihara and J. Onoe, "*Advances in Nuclear Fuel*" (S.T. Revanker ed.), InTech-Open Access Publisher, Chap. 4, pp. 73–94 (2012).

[28] A. Takashima, T. Nishii, and J. Onoe, *Int. J. Quantum Chem.* **109**, 2773 (2009).

[29] S. Watanabe *et al*., *J. Appl. Phys.* **119**, 235102 (2016).

[30] S. Watanabe *et al*., *AIP Adv.* **8,** 045221 (2018).

[31] S. Watanabe *et al*., *Chem. Phys. Lett.* **723**, 76 (2019).

[32] S. Watanabe *et al.*, *IOP Conf. Series*: *Mater. Sci. Eng.* **835**, 012001 (2020).

[33] S. Watanabe, Y. Inaba, M. Harigai, K. Takeshita, and J. Onoe, *Sci. Rep.* **12**, 5135 (2022).

[34] A. Rosén and D.E. Ellis, *J. Chem. Phys.* **62**, 3039 (1975).

[35] R.S. Mulliken, *J. Chem. Phys.* **23**, 1833; **23**, 1841; **23**, 2338; **23**, 2343 (1955).

[36] A. Rosén *et al.*, *J. Chem. Phys.* **65**, 3629 (1976).

[37] H. Nakamatsu, H. Adachi, and T. Mukoyama, *Bull. Inst. Chem. Res., Kyoto Univ.* **68**, 304 (1991).

[38] N. Mårtensson, P.A. Malmquist, S. Svensson and B. Johansson, *J. Chem. Phys.* **80**, 5458 (1984).

[39] U. Gelius, *J. Electron Spectrosc. Relat. Phenom.* **5**, 985 (1974).

[40] H. Nakamatsu, T. Mukoyama, and H. Adachi, *J. Electron Spectrosc. Relat. Phenom.* **53**, 265 (1991).

[41] J.J. Katz and E. Rabinowich eds, *The Chemistry of Uranium*, Vol. **5**, McGraw Hill (1951).

[42] G.L. DePoorter and C.K. Rofer-DePoorter, *Spectrosc. Lett.* **8**, 521 (1975).

[43] A.H. Lewis *et al*., *J. Chem. Phys*. **65**, 2707 (1976).

[44] J. Onoe *et al.*, *J. Phys. Soc. Jpn.* **63**, 3992 (1994).

[45] J. Onoe *et al*., *J. Phys. Soc. Jpn.* **65**, 2459 (1996).

[46] J. Onoe, *J. Phys. Soc. Jpn.* **66**, 2328 (1997).

[47] R. Paine *et al.*, *J. Chem. Phys*. **64**, 3081 (1976).

[48] B.J. Krohn, W.B. Person, and J. Overend, *J. Chem. Phys.* **65**, 969 (1976).

[49] L.H. Jones and S. Ekberg, *J. Chem. Phys*. **67**, 2591 (1977).

[50] W.R. Wadt and P.J. Hay, *J. Am. Chem. Soc.* **101**, 5198 (1979).

[51] D.H. Maylotte, R.L. Peters, and R.P. Messmer, *Chem. Phys. Lett.* **58**, 181 (1976).

[52] G.L. Gutsev and J. Russ, *Inorg. Chem*. **37**, 135 (1992).

[53] H. Becher *et al*., *J. Chem. Phys.* **100**, 1759 (1994).

[54] C. Marsden, *Chem. Commun*., 401 (1984).

[55] G.L. Gutsev, *Chem. Phys*. **179**, 325 (1994).

[56] J.C. Slater and K.H. Johnson, *Phys. Rev. B* **5**, 844 (1972).

[57] D.L. Hildenbrand, *J. Chem. Phys.* **66**, 4788 (1977).

[58] A.S. Baev *et al*., *Radiokhimiya* **28**, 460 (1986).

[59] P. Erode *et al.*, *The Physics of Actinides Compounds,* Plenum Press. New York (1983).

[60] H. Bethe, *Ann. Phys.* **3**, 133 (1929).

[61] J. Meyer *et al*., *Comput. Phys. Commun.* **54**, 55 (1989).

[62] T. Ejima *et al*., *Physica B* **186-188**, 77 (1993).

[63] G.H. Schadler, *Solid State Commun.* **74**, 1229 (1990).

[64] A.M. Holden, *Physical Metallurgy of Uranium*, Addison-Wesley, New York (1958).

[65] A.F. Fuggle *et al.*, *J. Phys. F* **4**, 335 (1974).

[66] H. Yamagami and A. Hasegawa, *J. Phys. Soc. Jpn.* **59**, 2426 (1990).

[67] P. Chiotti et al., IAEA *STI/PUB/424/5*, Vienna (1981).

[68] A.R. Kaufman, *Nuclear Reactor Fuel Elements*, Interscience/Butterworth, USA (1962).

[69] R.W. Buzzard, *Progress Report-Alloying Theory*, NBS-4032 (1955).

[70] J.J. Park and R.W. Buzzard, *TID-7526* (*Pt. 1*), 69 (1957).

[71] T. Ogawa *et al*., *J. Nucl. Mater.* **223**, 67 (1995).

[72] M. Hume-Rothery and G.W. Raynor, *Structure of Metals and Alloys,* Institute of Metals, London (1954).

[73] W.H. Zachariasen, *J. Inorg. Nucl. Chem.* **35**, 3487 (1973).

[74] L. Pauling, *The Nature of the Chemical Bond* (3rd ed.)*,* Cornell Univ. Press, New York (1960).

[75] G. Eriksson and K. Hack, *Metallur. Transact. B*, **21B**, 1013 (1990).

[76] M. Morinaga *et al*., *J. Phys. Soc. Jpn.* **53**, 653 (1984).
[77] M. Morinaga *et al*., *J. Phys. F, Met. Phys.* **15**, 1071 (1985).
[78] M. Morinaga *et al*., *Philos. Mag. A* **51**, 223 (1985).
[79] J. Onoe, *Quantum Chemistry*, Chap. **8**, Kindaikagakusha Press, Tokyo (2019) [*in Japanese*].
[80] J. Onoe *et al*., *Appl. Phys. Lett.* **82**, 595 (2003).
[81] J. Onoe *et al*., *J. Phys. Chem. Solids* **65**, 343 (2004).
[82] J. Onoe, A. Nakao, and A. Hida, *Appl. Phys. Lett.* **85**, 2741 (2004).
[83] T.A. Beu, J. Onoe, and A. Hida, *Phys. Rev. B* **72**, 155416 (2005).
[84] S. Ueda *et al*., *J. Phys. Chem. B* **110**, 22374 (2006).
[85] T.A. Beu and J. Onoe, *Phys. Rev. B* **74**, 195426 (2006).
[86] J. Onoe *et al*., *Phys. Rev. B* **75**, 233410 (2007).
[87] J. Onoe, T. Ito, and S. Kimura, *J. Appl. Phys.* **104**, 103706 (2008).
[88] A. Takashima, J. Onoe, and T. Nishii, *J. Appl. Phys.* **108**, 033514 (2010).
[89] A. Takashima, T. Nishii, and J. Onoe, *J. Phys. D*: *Appl. Phys*. **45**, 485302 (2012).
[90] S. Ryuzaki, M. Nishiyama, and J. Onoe, *Diamond & Relat. Mater.* **33**, 12 (2013).
[91] H. Masuda, J. Onoe, and H. Yasuda, *Carbon* **81**, 842 (2015).
[92] H. Masuda, H. Yasuda, and J. Onoe, *Carbon* **96**, 316 (2016).
[93] Y. Toda, S. Ryuzaki, and J. Onoe, *Appl. Phys. Lett.* **92**, 094102 (2008).
[94] H. Shima, H. Yoshioka, and J. Onoe, *Phys. Rev. B* **79**, 201401(R) (2009).
[95] H. Shima, H. Yoshioka, and J. Onoe, *Physica E* **42**, 1151 (2010).
[96] J. Onoe, A. Takashima and Y. Toda, *Appl. Phys. Lett.* 97, 241911 (2010).
[97] J. Onoe *et al*., *Fullerene, Nanotubes, and Carbon Nanostructures* **20**, 1 (2012) [Invited paper].
[98] J. Onoe *et al*., *J. Phys.*: *Condens. Matter* **24**, 175405 (2012).
[99] J. Onoe *et al*., *Europhys. Lett.* **98**, 27001 (2012).
[100] S. Ryuzaki and J. Onoe, *Appl. Phys. Lett*. **104**, 113301 (2014).
[101] S. Ono, Y. Toda, and J. Onoe, *Phys. Rev. B* **90**, 155435 (2014).
[102] M. Nakaya, S. Watanabe, and J. Onoe, *Carbon* **152**, 882 (2019).
[103] H. Ueno *et al.*, *Fullerene Sci. Technol.* **6**, 319 (1998).
[104] M. Igami, T. Nakanishi, and T. Ando, *J. Phys. Soc. Jpn.* **68**, 716 (1999).
[105] J.C. Charlier, T.W. Ebbesen, and Ph. Lambin, *Phys. Rev. B* **53**, 11108 (1996).
[106] H. Matsumura and T. Ando, *J. Phys. Soc. Jpn.* **67**, 3542 (1998).
[107] R. Maruyama, *J. Appl. Phys.* **94**, 6871 (2003).
[108] G. Wang, Y. Li, and Y. Huang, *J. Phys. Chem. B* **109**, 10957 (2005).

[109] K. Momma and F. Izumi, *J. Appl. Crystallogr.* **41**, 653 (2008).
[110] R.K. Kremer, *Appl. Phys. A*: *Solids Surf*. **56**, 211 (1993).
[111] S. Kitagawa, R. Kitaura, and S. Noro, *Angew. Chem. Int. Ed.* **43**, 2334 (2004).
[112] H. Yi *et al.*, *Adv. Funct. Mater*. **31**, 2006970 (2021).
[113] B. Bornamehr *et al*., *J. Mater. Chem. A* **11**, 10473 (2023).
[114] A. Gotoh *et al*., *Nanotechnology* **18**, 345609 (2007).
[115] J. Lehto, S. Haukka, and R. Harjula, *J. Chem. Soc. Dalton Trans*., 1007 (1990).
[116] N. L. Torad *et al.*, *J. Mater. Chem.* **22**, 18261 (2012).
[117] H. Tokoro and S. Ohkoshi, *Bull. Chem. Soc. Jpn.* **88**, 227 (2015).
[118] K. Uruga *et al*., *J. Nucl. Sci. Technol.* **44**, 1024 (2007).
[119] A. N. Caruso *et al.*, *Phys. Rev. B* **79**, 195202 (2009).
[120] D. S. Middlemiss, and C. C. Wilson, *Phys. Rev. B* **77**, 155129 (2008).
[121] J. C.Wojdeł *et al*., *J. Chem. Phys*. **128**, 044713 (2008).
[122] J.C. Wojdeł, *J. Mol. Model.* **15**, 567 (2009).
[123] J.J.C. Wojdeł *et al.*, *J. Mater. Chem.* **19**, 2032 (2009).
[124] K. Ogasawara *et al*., *Phys. Rev. B* **64**, 115413 (2001).
[125] K. Ogasawara *et al*., *J. Solid State Chem*. **178**, 412 (2005).
[126] S. Watanabe *et al*., *Phys. Rev. B* **79**, 075109 (2009).
[127] S. Watanabe *et al*., *Phys. Rev. B* **81**, 125128 (2010).
[128] Y. Obukuro *et al*., *Solid State Commun*. **206**, 42 (2015).
[129] M. C. Payne *et al.*, *Rev. Mod. Phys.* **64**, 1045 (1992).
[130] M. D. Segall *et al*., *J. Phys.*: *Condens. Matter* **14**, 2717 (2002).
[131] S. J. Clark *et al*., *Z. Kristallogr.* **220**, 567 (2005).
[132] A. H. MacDonald, and S. H. Vosko, *J. Phys. C*: *Solid State Phys*. **12**, 2977 (1979).
[133] B. G. Breit, *Phys. Rev*. **34**, 553 (1929).
[134] B. G. Breit, *Phys. Rev.* **39**, 616 (1932).
[135] S. Sugano, Y. Tanabe, and H. Kamimura, *Multiplets of Transition-Metal Ions in Crystals*, Academic, New York (1970).
[136] A. Ito, M. Suenaga, and K. Ono, *J. Chem. Phys*. **48**, 3597 (1968).
[137] J. C. Slater, *Quantum Theory of Molecules and Solids*, Vol. 4, McGraw-Hill, New York (1974).
[138] H.J. Ache *et al*., *IAEA Tech. Rep*. No. **308** (1989).
[139] H. Asano and M. Aritomi, *J. Nucl. Sci. Technol.* **42**, 470 (2005).
[140] O. Tochiyama and S. Masuda, *J. Nucl. Sci. Technol.* **50**, 665 (2013).

[141] A.H. Gallardo, T. Matsuzaki, and H. Aoki, *Energy Policy*, **73**, 391 (2014).

[142] J. Onoe *et al*., *RSC Adv.* **11**, 20701 (2021).

[143] P.K. Verna, R.B. Gujai, and P.K. Mohapatra, *Radiochim. Acta* **107**, 423 (2019).

[144] A.C. Samuels *et al*., *Inorg. Chem.* **53**, 12315 (2014).

[145] M.J. Frisch, G.W. Trucks, H.B. Schlegel, G.E. Scuseria, M.A. Robb, J.R. Cheeseman, G. Scalmani, V. Barone, G.A. Petersson, H. Nakatsuji, X. Li, M. Caricato, A.V. Marenich, J. Bloino, B.G. Janesko, R. Gomperts, B. Mennucci, H.P. Hratchian, J.V. Ortiz, A.F. Izmaylov, J.L. Sonnenberg, D. Williams-Young, F. Ding, F. Lipparini, F. Egidi, J. Goings, B. Peng, A. Petrone, T. Henderson, D. Ranasinghe, V.G. Zakrzewski, J. Gao, N. Rega, G. Zheng, W. Liang, M. Hada, M. Ehara, K. Toyota, R. Fukuda, J. Hasegawa, M. Ishida, T. Nakajima, Y. Honda, O. Kitao, H. Nakai, T. Vreven, K. Throssell, J.A. Montgomery, Jr., J.E. Peralta, F. Ogliaro, M.J. Bearpark, J.J. Heyd, E.N. Brothers, K.N. Kudin, V.N. Staroverov, T.A. Keith, R. Kobayashi, J. Normand, K. Raghavachari, A.P. Rendell, J.C. Burant, S.S. Iyengar, J. Tomasi, M. Cossi, J.M. Millam, M. Klene, C. Adamo, R. Cammi, J.W. Ochterski, R.L. Martin, K. Morokuma, O. Farkas, J.B. Foresman, and D.J. Fox, *Gaussian 16*, *Revision C.01*, Gaussian Inc., Wallingford CT (2016).

[146] G. Kresse and J. Furthmüller, *Phys. Rev. B* **54**, 11169 (1996).

[147] G. Kresse and D. Joubert, *Phys. Rev. B* **59**, 1758 (1999).